



# Contributions of the LOFAR Cosmic Ray Key Science Project to the 35th International Cosmic Ray Conference (ICRC 2017)

A. Bonardi<sup>1</sup>, S. Buitink<sup>2</sup>, A. Corstanje<sup>1</sup>, H. Falcke<sup>1,3,4</sup>, B. M. Hare<sup>5</sup>,  
J. R. Hörandel<sup>1,3</sup>, P. Mitra<sup>2</sup>, K. Mulrey<sup>2</sup>, A. Nelles<sup>1,6</sup>, J. P. Rachen<sup>1</sup>,  
L. Rossetto<sup>1</sup>, P. Schellart<sup>1,7</sup>, O. Scholten<sup>5,8</sup>, S. ter Veen<sup>1,4</sup>, S. Thoudam<sup>1,9</sup>,  
T. N. G. Trinh<sup>5</sup>, T. Winchen<sup>2</sup>

<sup>1</sup> Department of Astrophysics/IMAPP, Radboud University Nijmegen, P.O. Box 9010, 6500 GL, Nijmegen, The Netherlands,

<sup>2</sup> Astrophysical Institute, Vrije Universiteit Brussel, Pleinlaan 2, 1050 Brussels, Belgium,

<sup>3</sup> NIKHEF, Science Park Amsterdam, 1098 XG Amsterdam, The Netherlands,

<sup>4</sup> Netherlands Institute of Radio Astronomy (ASTRON), Postbus 2, 7990 AA Dwingeloo, The Netherlands,

<sup>5</sup> KVI-CART, University Groningen, P.O. Box 72, 9700 AB Groningen,

<sup>6</sup> Department of Physics and Astronomy, University of California Irvine, Irvine, CA 92697-4575, USA,

<sup>7</sup> Department of Astrophysical Sciences, Princeton University, Princeton, NJ 08544, USA,

<sup>8</sup> Interuniversity Institute for High-Energy, Vrije Universiteit Brussel, Pleinlaan 2, 1050 Brussels, Belgium,

<sup>9</sup> Department of Physics and Electrical Engineering, Linnéuniversitetet, 35195 Växjö, Sweden

## Contents

Cosmic ray mass composition with LOFAR . . . . .	3
Characterisation of the radio frequency spectrum emitted by high energy air showers with LOFAR . . . . .	11
The effect of the atmospheric refractive index on the radio signal of ex- tensive air showers using Global Data Assimilation System (GDAS) . .	19
Circular polarization in radio emission from extensive air showers . . . . .	27
Circular polarization of radio emission from extensive air showers probes atmospheric electric fields in thunderclouds. . . . .	35
Study of the LOFAR radio self-trigger and single-station acquisition mode . . . . .	43
Expansion of the LOFAR Radboud Air Shower Array . . . . .	51
Overview and Status of the Lunar Detection of Cosmic Particles with LOFAR . . . . .	59

# Cosmic ray mass composition with LOFAR

---

**S. Buitink<sup>\*1</sup>, A. Bonardi<sup>2</sup>, A. Corstanje<sup>2</sup>, H. Falcke<sup>2,3,4</sup>, B. M. Hare<sup>5</sup>, J. R. Hörandel<sup>1,3</sup>,  
P. Mitra<sup>1</sup>, K. Mulrey<sup>1</sup>, A. Nelles<sup>2,6</sup>, J. P. Rachen<sup>2</sup>, L. Rossetto<sup>2</sup>, P. Schellart<sup>2,8</sup>,  
O. Scholten<sup>5,7</sup>, S. ter Veen<sup>2,4</sup>, S. Thoudam<sup>2,9</sup>, T. N. G. Trinh<sup>5</sup>, and T. Winchen<sup>1</sup>**

<sup>1</sup>*Astrophysical Institute, Vrije Universiteit Brussel, Pleinlaan 2, 1050 Brussels, Belgium*

<sup>2</sup>*Department of Astrophysics / IMAPP, Radboud University, P.O. Box 9010, 6500 GL Nijmegen, The Netherlands*

<sup>3</sup>*NIKHEF, Science Park Amsterdam, 1098 XG Amsterdam, The Netherlands*

<sup>4</sup>*Netherlands Institute of Radio Astronomy (ASTRON), Postbus 2, 7990 AA Dwingeloo, The Netherlands*

<sup>5</sup>*KVI-CART, University Groningen, P.O. Box 72, 9700 AB Groningen, The Netherlands*

<sup>6</sup>*Department of Physics and Astronomy, University of California Irvine, Irvine, CA 92697-4575, USA*

<sup>7</sup>*Interuniversity Institute for High-Energy, Vrije Universiteit Brussel, Pleinlaan 2, 1050 Brussels, Belgium*

<sup>8</sup>*Department of Astrophysical Sciences, Princeton University, Princeton, NJ 08544, USA*

<sup>9</sup>*Department of Physics and Electrical Engineering, Linné Universitetet, 35195 Växjö, Sweden*

*E-mail: [Stijn.Buitink@vub.be](mailto:Stijn.Buitink@vub.be)*

The LOFAR radio telescope measures the radio emission from extensive air showers with unprecedented precision. In the dense core individual air showers are detected by hundreds of dipole antennas. By fitting the complex radiation pattern to Monte Carlo radio simulation codes we obtain measurements of the atmospheric depth of the shower maximum  $X_{\max}$  with a precision of  $< 20 \text{ g/cm}^2$ . This quantity is sensitive to the mass composition of cosmic rays.

We discuss the first mass composition results of LOFAR and the improvements that are currently being made to enhance the accuracy of future analysis. Firstly, a more realistic treatment of the atmosphere will decrease the systematic uncertainties due to the atmosphere. Secondly, a series of upgrades to the LOFAR system will lead to increased effective area, duty cycle, and the possibility to extend the composition analysis down to the energy of  $10^{16.5} \text{ eV}$ .

*35th International Cosmic Ray Conference – ICRC2017*

*10-20 July, 2017*

*Bexco, Busan, Korea*

---

<sup>\*</sup>Speaker.

## 1. Introduction

Radio detection of air showers [1] is a rapidly developing technique, that offers promising possibilities to accurately measure the air shower energy and the atmospheric depth of the shower maximum, known as  $X_{\max}$  [2, 3]. The technique can be used in combination with established techniques such as fluorescence detection and surface detection. Dense antenna arrays like the core of LOFAR [4], or the low-frequency part of the future SKA observatory [5], are useful for detailed verification of our understanding of the emission mechanism and the accuracy of radio simulation codes. Moreover, they allow  $X_{\max}$  measurements with a precision of  $<20 \text{ g/cm}^2$  or even better [6]. The dense antenna distribution comes at the expense of a limited instrumented area, which leaves a study of ultra-high-energy cosmic rays up to the cut-off out of reach. However, air shower measurements with LOFAR and SKA are of particular interest for mass composition studies at energies between the second knee and the ankle [7, 8].

LOFAR is a digital radio telescope constructed in the Netherlands with satellite stations across Europe. It consists of thousands of dipole antennas, operating in the frequency range of 10 – 240 MHz. It produces extremely detailed air shower radio data, by using the dense core region, or *superterp*, where 384 antennas are located within a circle of 320 m diameter. A particle array, LORA [9], has been installed on the superterp and is used for triggering and reconstruction. Each antenna contains a ring buffer which is read-out in case of a trigger. The full waveform is stored for offline analysis [10].

The radio emission of air showers results from a combinations of geomagnetic and charge excess radiation. To correctly calculate it, it is also needed to take into account the relativistic propagation effects due to the small but finite refractivity of air (see references in [1]). The interference of these contributions causes an azimuthal asymmetry of the distribution of radio power on the ground. It is also the cause of the location-dependent polarization angle [11] and even a small but measurable amount of circular polarization [12]. To reach a high precision reconstruction of the air shower a two-dimensional fit is developed that takes into account the asymmetrical nature of the emission [3]. The first LOFAR composition results based on this method are shown in Fig. 2 [13].

The largest systematic uncertainty in the LOFAR  $X_{\max}$  reconstruction is due to effects of the variation of the index of refraction in air [13, 14, 16]. In previous studies, we relied on CORSIKA [17] simulations using the US Standard Atmosphere. Furthermore, the radio emission code CoREAS [18] internally uses a linear scaling of the refractivity with air density, only accepting a variable ground level value for the index of refraction as input. In reality though, the refractivity depends on the relative humidity, which can vary significantly with altitude.

In order to reduce the uncertainties, we have developed a tool that extracts realistic profiles for the air density and index of refraction as a function of atmospheric depth. An upcoming release of CORSIKA will include this code as well as adaptations that make it easy to run CORSIKA/CoREAS with these additional input files. We have revised our simulation pipeline and plan to soon start new simulation production based on this and other improvement. In these proceedings we describe the updated simulation pipeline and other future improvements to LOFAR cosmic-ray detection.

## 2. Simulation pipeline

Reconstruction of air showers with LOFAR is based on the production of dedicated sets of simulations for each detected high-quality air shower<sup>1</sup>. There are two reasons for this. Firstly, the shape of the radio profile on the ground depends not only on the azimuth and zenith angle, but also on the angle with the geomagnetic field. Parametrizations of these profiles exist but will not yield the same resolution on  $X_{\max}$  that full simulations provide [19].

Secondly, LOFAR antennas are not placed on a regular grid but in dense rings with spacings in between. This makes it nearly impossible to construct criteria on the energy, core location and arrival direction for which a 100% detection efficiency is reached. Instead of defining such criteria, we evaluate for each measured shower whether or not the detection efficiency is near 100%. This is done by creating a set of CORSIKA showers that have the same energy, arrival direction and core position, but cover the natural range of  $X_{\max}$  values. Only if all showers in the set trigger LORA and pass the high-quality criterium, the shower is included in the mass composition analysis.

The number of simulations needed to reconstruct the shower and evaluate a possible composition bias is optimized with CONEX [20], which allows us to quickly produce the longitudinal profiles for hundreds of showers. Now, it is possible to select a subset of these showers for subsequent full CORSIKA simulation. We choose this subset by first selecting the two proton showers with the highest and lowest value for  $X_{\max}$ . Then, we select nine more proton showers with intermediate values, (nearly) equally spaced between the extreme values. Since the range of  $X_{\max}$  values for iron showers is much narrower, we select a total of five iron showers using the same algorithm. This procedure assures that the simulation set can be used for the bias test.

Finally we add eleven additional shower simulations close to the estimated  $X_{\max}$  of the measured shower to increase the resolution of the reconstruction. This estimation is given by fitting a parametrization of the radio signal [19] to the data, that has a resolution of  $\sim 40 \text{ g/cm}^2$ .

Another advantage of having dedicated sets of simulations per shower is that we can use atmospheric description that closely match the conditions during the actual measurement, instead of profiles that are averaged over years or months. In particular, the radio emission is sensitive to fluctuations in the humidity which change over much shorter time scales. The up-to-date profiles are based on data from GDAS [15] and a detailed description of the procedure can be found elsewhere in these proceedings [16].

The radio emission is simulated for antennas in a star-shaped pattern in the shower plane. The LOFAR low-band antenna model is applied to the simulated electric fields to calculate the measured signals in the two dipoles. The measured pulse power is defined as the total power in a 55 ns window centered around the pulse maximum, summed over both polarisations. Finally, a two-dimensional map of the pulse power is created by interpolating the star-shaped pattern. More details are found in [3].

A GEANT4 simulation is used to calculate the lateral distribution of the energy deposited in the LORA scintillators. These simulations are needed to test whether all simulated showers would indeed trigger the LORA detector. They are also included in the shower reconstruction.

---

<sup>1</sup>High-quality currently means that at least four rings of LOFAR low-band antennas should be able to independently reconstruct the shower direction that is in agreement with the LORA particle reconstruction. However, this requirement could be relaxed in the future.

### 3. Reconstruction

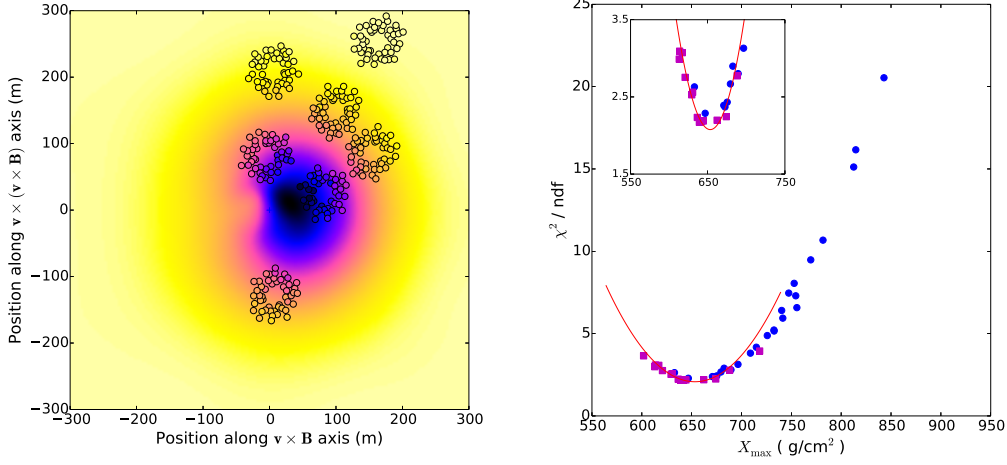


**Figure 1:** Left: event reconstruction. The small circles indicate LOFAR antenna positions (grouped in larger circles) projected into the shower plane. Their color indicates the measured power of the radio pulse. The background is the two-dimensional simulated radio power map. The fit quality is high when the colors inside the circles blend into the background. Right: reconstruction of  $X_{\max}$ . Every data point corresponds to a single simulated shower. Together they form the dedicated simulation set produced for this particular shower. The reduced  $\chi^2$  of the fit is plotted against  $X_{\max}$  and a parabola is fitted to find the optimum  $X_{\max}$ . The inlay is a zoomed-in version of the minimum of the curve demonstrating its sharpness. Purple squares correspond to iron showers and blue circles to proton showers.

The radio and particle profiles are fitted to the data simultaneously. The fit has four free parameters: two for the shower core position and scaling parameters for both the radio and the particle profiles. Inclusion of the particle data in the fit does not have much effect on the fitted core position in practice. However, it acts as an additional consistency check and sets the energy scale. The analysis presented here does not yet include the absolute calibration of the antennas [21] so the scaling parameter for the radio power has an arbitrary value. In effect, the ratio of two scaling parameters also has an arbitrary but constant value. The width of the distribution of this parameter is a measure for the energy resolution of the reconstruction, which is 32%.

The reduced  $\chi^2$  of the fit is very sensitive to  $X_{\max}$  as is seen in Fig. 1. The minimum of the  $\chi^2$ -curve is found by fitting a parabola to the points near the lowest value. The curve is not smooth because shower-to-shower fluctuations other than variations in  $X_{\max}$ . In order to obtain a robust parabola fit, data points that have neighbours on *both* sides that have a lower  $\chi^2$ -value are excluded from the fit. Monte Carlo simulations have shown that this produces a significant increase in  $X_{\max}$  resolution.

### 4. Results

The two main results from the first LOFAR composition analysis are shown in Fig. 2. The left panel displays the LOFAR  $X_{\max}$  measurements in comparison with other experiments based

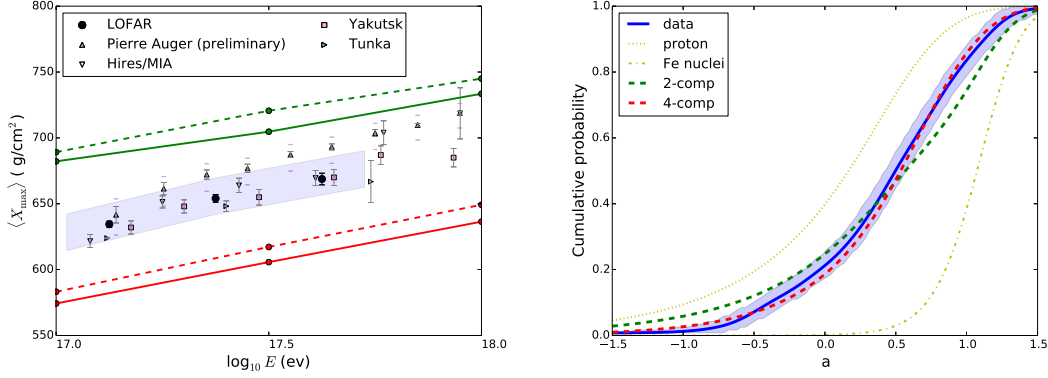


**Figure 2:** Left: mean  $X_{\max}$  as a function of energy. The LOFAR results are in agreement with results based on different techniques within systematic uncertainties (Auger systematic uncertainties are indicated with purple bars [22]). The green lines are for pure proton composition and the red lines for pure iron (dashed: EPOS-LHC, solid: QGSJETII). Right: cumulative distribution of  $a$  for LOFAR data (blue; with  $1\sigma$  uncertainty band) and different compositions. A four-component model is required to reproduce the data.

on other techniques. The error bars represent  $1\sigma$  statistical uncertainties and the shaded region indicates the systematic uncertainty.

The right panel shows the cumulative distribution of  $a$ , a parameter that indicates the position of the  $X_{\max}$  value of a particular shower relative to the simulated mean for pure proton ( $a = 0$ ) and pure iron ( $a = 1$ ) lines. A pure proton composition would yield a broad distribution of  $a$  around  $a = 0$ , while a pure iron composition corresponds to a narrow distribution around  $a = 1$ . The measured distribution can now be fitted with multi-component models. The minimum number of components required to achieve a good fit is four (proton, helium, nitrogen, iron). A full scan of the allowed parameter space yields a large contribution of light elements. Although there is a large uncertainty in the contribution of individual elements, the total fraction of light elements (p+He) is well constrained. It has a best fit value of 0.8 and lies within the range [0.38,0.98] at a 99% confidence level for QGSJETII. More details are found in [13].

## 5. Systematic uncertainties due to the atmosphere

As mentioned above, the systematic uncertainty on  $X_{\max}$  is currently dominated by atmospheric uncertainties. Fluctuations in air density and humidity reduce the resolution on  $X_{\max}$ . Moreover, since the original simulations used an index of refraction on ground level that corresponds to 0% relative humidity, the reconstructed value for  $X_{\max}$  is expected to shift to larger values for realistic atmospheres. In the original analysis, this led to an asymmetric total systematic uncertainty of +14/-10  $\text{g/cm}^2$ .

Interestingly, another contribution to the total systematic uncertainty is an observed zenith dependence on the mean value of  $X_{\max}$ . Since this can also be the result of using inaccurate atmospheric profiles, this dependence may reduce for the new simulations based on GDAS profiles. Indeed, this would be a confirmation that the new profiles are more realistic than the older. A more detailed account on the various systematic uncertainties is found in [13].

## 6. Future extensions

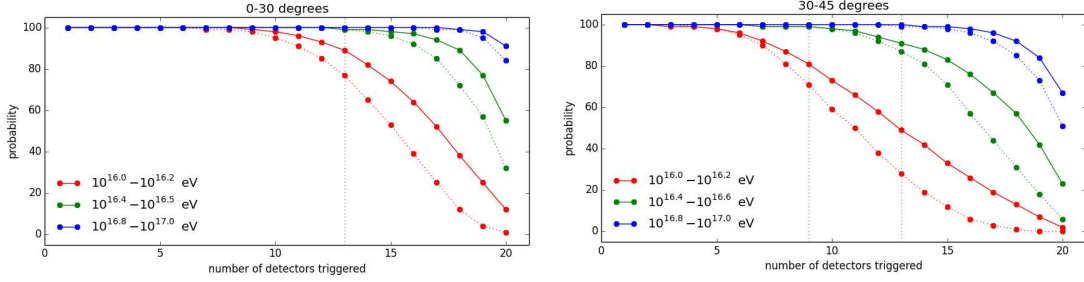


**Figure 3:** Detection probability for proton showers (solid) and iron showers (dotted) for different energies and zenith angles, as a function of number of particle detectors required for a trigger. In a hybrid triggering scheme, a detection efficiency of 100% down to  $10^{16.5}$  eV is achieved by reducing the amount of required triggers. The precise amount depends on the area under consideration. For this plot only showers having a core inside the superterp, i.e. within 160 m of the LORA core, are considered.

The improved simulation pipeline is expected to yield more accurate measurements of  $X_{\max}$ , but the composition analysis still suffers from low statistics. For the (near) future, several upgrades are planned that will increase the number of unbiased showers.

- **LORA expansion** Twenty more particle detectors will be installed at five LOFAR stations (rings of antennas) near the superterp. This will both increase the effective area by a factor of  $\sim 40\%$  and allow triggering on a specific class of showers for which the superterp is located outside of the Cherenkov angle. Here, the radio signal quickly becomes weaker but may be more sensitive to the precise longitudinal evolution of a shower. The data will be used to study the possibility of determining more shower evolution parameters than only  $X_{\max}$ , which could both be useful for composition studies and constraining hadronic interaction models. This can be regarded as a first step towards shower radio tomography, which has been proposed for SKA<sup>2</sup>. More details on the expansion are found elsewhere in these proceedings [23]
- **Hybrid triggering** The current triggering system requires 13 out of 20 LORA detectors to trigger. This has two disadvantages. First, while this setting yields a near 100% detection efficiency for showers above  $10^{17}$  eV, most of the triggers are from showers that are of much lower energy and do not produce an observable radio pulse. Indeed, in 80% of the data that is stored, no radio signal is found. Secondly, nearly half of the high-quality showers for which we can reconstruct  $X_{\max}$  fall in the  $10^{16.5} - 10^{17}$  eV energy range, where the detection efficiency is too small to allow for an unbiased composition study.

Both problems are resolved simultaneously by implementing a hybrid triggering system that combines information from the particles detectors and radio antennas in real-time. Through continuous monitoring of each antenna data stream it is possible to send trigger messages to the central LORA computer for each radio peak that is above the noise background by a

<sup>2</sup>Apart from being a larger and more regularly spaced array, SKA-low has the additional advantage that it will be sensitive to smaller sub-structures in the shower because of its increased frequency range (50-350 MHz).



certain threshold value. In the LORA computer the messages of all antennas are collected and combined with the data from the particle detectors. A hybrid trigger is issued when both a minimum number of antennas and a minimum number of particle detectors show a signal-over-threshold.

Since every hybrid trigger has a visible radio signal we boost our fraction of useful data from 20% to nearly 100%. At the same time, the risk of triggering on manmade impulsive signals is extremely low since we require coincidence with a particle signal. Even more importantly, we can now lower the required number of particle detectors for a trigger. This means we will be able to detect cosmic ray below  $10^{17}$  eV bias-free, reducing our energy threshold for the mass composition analysis.

Figure 3 shows a simulation study of the detection probability for proton showers (solid lines) and iron showers (dotted lines) for different energy ranges. A bias-free sample is achieved when the proton and iron lines overlap, which only happens when both species reach a probability of nearly 100%. This preliminary study indicates the energy range for mass composition studies can be extended to at least  $10^{16.5}$  eV, by reducing the required number of detector for triggering.

- **LOFAR 2.0** An often advertised advantage of radio detection of air showers is the larger duty cycle of nearly 100%. However, due to technical and organizational aspects, LOFAR reaches a duty cycle of only 10-20%. Although air shower detection always run in the background of astronomical observations, there are gaps between these observations. Moreover, more than half of the observations use the high-band antennas, which are of very limited use to air shower analysis [24]. LOFAR 2.0 is a planned upgrade to the observatory that will allow a more simultaneous measurement modes. From a technical side, it will become possible to use low and high band antennas at the same time. Furthermore, observation scheduling will done in a manner that takes advantage of the possibilities of a digital radio telescope. Observations will be able to run in parallel with different start and end times. These changes will make it possible to perform low-band air-shower measurements continuously, improving the duty cycle considerably.

## 7. Conclusions

LOFAR measures the atmospheric depth of the shower maximum  $X_{\max}$  with a precision of  $< 20$  g/cm<sup>2</sup> using a technique based on two-dimensional reconstruction of the radiation profile. The first mass composition results are in agreement with measurements based on other techniques and consistent with a strong light-mass component below the ankle. To further optimize the precision and reduce systematic uncertainties, a new simulation pipeline is being developed that incorporates realistic atmospheric profiles. Furthermore, future upgrades are planned that improve the performance of cosmic ray detection with LOFAR, increasing the effective area and duty cycle, and reducing the energy threshold for mass composition analysis.

## Acknowledgements

The LOFAR cosmic ray key science project acknowledges funding from an Advanced Grant of the European Research Council (FP/2007-2013) / ERC Grant Agreement n. 227610. The project has also received funding from the European Research Council (ERC) under the European Union's Horizon 2020 research and innovation programme (grant agreement No 640130). We furthermore acknowledge financial support from FOM, (FOM-project 12PR3041-3) and NWO (Top Grant 614-001-454, and Spinoza Prize SPI 78-409). AN is supported by the DFG (research fellowship NE 2031/1-1). LOFAR, the Low Frequency Array designed and constructed by ASTRON, has facilities in several countries, that are owned by various parties (each with their own funding sources), and that are collectively operated by the International LOFAR Telescope foundation under a joint scientific policy.

## References

- [1] T. Huege, *Physics Reports* **620**, 1-52 (2016).
- [2] W. Apel *et al.* [LOPES], *Phys. Rev. D* **90**, 062001 (2014).
- [3] S. Buitink *et al.* [LOFAR], *Phys. Rev. D* **90**, 082003 (2014).
- [4] M. P. van Haarlem *et al.* [LOFAR], *Astron. & Astrophys.* **556**, A2 (2013).
- [5] T. Huege *et al.* [SKA High Energy Cosmic Particle Focus Group], AASKA14, 148 (2015).
- [6] A. Zilles, S. Buitink, and T. Huege, these proceedings (2017).
- [7] K.-H. Kampert and M. Unger, *Astropart. Phys.* **35**, 660 (2012).
- [8] S. Thoudam *et al.*, *Astron. & Astrophys.* **595**, A33 (2016).
- [9] S. Thoudam *et al.*, [LOFAR], *Nucl. Instr. and Meth. in Phys. Res. A* **767**, 339 (2014).
- [10] P. Schellart *et al.* [LOFAR], *Astron. & Astrophys.* **560**, A98 (2013).
- [11] P. Schellart *et al.* [LOFAR], *J. Cosmology Astropart. Phys.* **10**, 014 (2014).
- [12] O. Scholten *et al.* [LOFAR], *Phys. Rev. D* **94**, 103010 (2016).
- [13] S. Buitink *et al.* [LOFAR], *Nature* **531**, 70-73 (2016).
- [14] A. Corstanje *et al.* [LOFAR], *Astropart. Phys.* **89**, 23 (2017).
- [15] NOAA Air Resources Laboratory (ARL), Global Data Assimilation System (GDAS1) Archive Information, Tech. rep. (2004).
- [16] P. Mitra *et al.* [LOFAR], these proceedings (2017).
- [17] D. Heck, Report FZKA **6019** (1998).
- [18] T. Huege, M. Ludwig, and C. James, *AIP Conference Proceedings* **1535**, 128-132 (2012).
- [19] A. Nelles *et al.* [LOFAR], *J. Cosm. Astropart. Phys.* **5**, 18 (2015).
- [20] T. Bergmann *et al.*, *Astropart. Phys.* **26**, 420-432 (2007).
- [21] A. Nelles *et al.* [LOFAR], *JINST* **10**, P11005 (2015).
- [22] A. Porcelli *et al.* [Pierre Auger Collaboration], PoS (ICRC2015) 420; arXiv:1509.03732 (2015).
- [23] K. Mulrey *et al.* [LOFAR], these proceedings (2017).
- [24] A. Nelles *et al.* [LOFAR], *Astropart. Phys.* **65**, 11 (2015).

# Characterisation of the radio frequency spectrum emitted by high energy air showers with LOFAR

---

**L. Rossetto<sup>\*1</sup>, A. Bonardi<sup>1</sup>, S. Buitink<sup>2</sup>, A. Corstanje<sup>1</sup>, H. Falcke<sup>1,3,4</sup>, B.M. Hare<sup>5</sup>, J.R. Hörandel<sup>1,3</sup>, P. Mitra<sup>2</sup>, K. Mulrey<sup>2</sup>, A. Nelles<sup>1,6</sup>, A. Olid Gonzalez<sup>1</sup>, J.P. Rachen<sup>1</sup>, P. Schellart<sup>1,7</sup>, O. Scholten<sup>5,8</sup>, S. ter Veen<sup>1,4</sup>, S. Thoudam<sup>1,9</sup>, T.N.G. Trinh<sup>5</sup>, T. Winchen<sup>2</sup>**

<sup>1</sup> *Department of Astrophysics/IMAPP, Radboud University, P.O. Box 9010, 6500 GL Nijmegen, The Netherlands*

<sup>2</sup> *Astrophysical Institute, Vrije Universiteit Brussel, Pleinlaan 2, 1050 Brussels, Belgium*

<sup>3</sup> *NIKHEF, Science Park Amsterdam, 1098 XG Amsterdam, The Netherlands*

<sup>4</sup> *Netherlands Institute of Radio Astronomy (ASTRON), Postbus 2, 7990 AA Dwingeloo, The Netherlands*

<sup>5</sup> *KVI-CART, University Groningen, P.O. Box 72, 9700 AB Groningen, The Netherlands*

<sup>6</sup> *Department of Physics and Astronomy, University of California Irvine, Irvine, CA 92697-4575, USA*

<sup>7</sup> *Department of Astrophysical Sciences, Princeton University, Princeton, NJ 08544, USA*

<sup>8</sup> *Interuniversity Institute for High-Energy, Vrije Universiteit Brussel, Pleinlaan 2, 1050 Brussels, Belgium*

<sup>9</sup> *Department of Physics and Electrical Engineering, Linnéuniversitetet, 35195 Växjö, Sweden*

*E-mail: [l.rossetto@astro.ru.nl](mailto:l.rossetto@astro.ru.nl)*

The high number density of radio antennas at the LOFAR core in Northern Netherlands allows to detect radio signals emitted by extensive air showers in the energy range  $10^{16} - 10^{18}$  eV, and to characterise the geometry of the observed cascade in a detailed way. The radio signal emitted by extensive air showers along their propagation in the atmosphere has been studied in the 30 – 70 MHz frequency range. The study has been conducted on real data and simulated showers. Regarding real data, cosmic ray radio signals detected by LOFAR since 2011 have been analysed. For simulated showers, the CoREAS code, a plug-in of the CORSIKA particle simulation code, has been used. The results show a clear dependence of the frequency spectrum on the distance to the shower axis for both real data and simulations. In particular, the spectrum flattens at a distance around 100 m from the shower axis, where the coherence of the radio signal is maximum. This behaviour could also be used to reconstruct the position of the shower axis at ground. A correlation between the frequency spectrum and the geometrical distance to the depth of the shower maximum  $X_{\text{max}}$  has also been investigated. The final aim of this study is to find a method to improve the inferred information of primary cosmic rays with radio antennas, in view of affirming the radio detection technique as reliable method for the study of extensive air showers.

*35<sup>th</sup> International Cosmic Ray Conference,  
12 – 20 July, 2017  
Bexco, Busan, Korea*

---

<sup>\*</sup>Speaker.

## 1. Introduction

Radio emission from Extensive Air Showers (EAS) was detected for the first time by Jelley et al. in 1965 [1]. Since 2005 radio experiments like CODALEMA [2] and LOPES [3] started detecting air showers up to an energy of  $10^{18}$  eV, confirming the radio emission mechanisms of cosmic rays in the Earth atmosphere. Measurements performed in the last years by the LOFAR experiment [4], the Auger Engineering Radio Array of the Pierre Auger Observatory (AERA) [5], and the Tunka-Rex radio array [6] have greatly improved the understanding of radio emission processes of extensive air showers. First studies of radio frequency spectra below 100 MHz were conducted in late 1960s and early 1970s [7]. Analytical calculations [8, 9] and simulation studies [10] conducted at the beginning of years 2000s indicated a dependence of the radio frequency spectrum on cosmic ray air shower characteristics. Furthermore, recent analysis conducted at AERA shows a dependence of the frequency spectrum on primary particle properties [11]. This demonstrates that it is feasible to extrapolate information from the frequency spectrum with the current radio antenna arrays.

A detailed study for characterising the pattern of the radio frequency spectrum and studying its correlation with the primary cosmic ray features has been conducted with LOFAR. Among radio experiments, LOFAR is the one with the densest number of antennas, thus the most suitable for this kind of analysis. In order to find the best parameters which describe the correlation between primary cosmic rays and the emitted radio signals, data collected by LOFAR since 2011 have been studied in the 30 – 70 MHz frequency range. Results obtained on real data have been cross-checked with simulations.

## 2. The LOw Frequency ARray

The LOw Frequency ARray (LOFAR) is a radio antenna array which consists of 50 stations in Northern Europe with a denser core in the Northern Netherlands. Each Dutch station consists of 96 Low Band Antennas (LBAs) and 48 High Band Antennas (HBAs) which operate in the frequency range 10 – 90 MHz and 110 – 240 MHz, respectively. The 24 stations which form the LOFAR core are located in the Northern Netherlands, and cover a circle of approximately 2 km radius. In the central area, six stations, also called *Superterp*, are located in a circular area of roughly 320 m diameter, and form the densest area of antennas. The layout of LOFAR central stations is shown in figure 1, together with a picture of one LBA. The LOFAR central array is also instrumented with 20 scintillator detectors, the LORA array [12]. Triggers for cosmic ray data acquisition are provided by LORA, which also permits the reconstruction of the arrival direction and energy of primary particles. In the current configuration the LOFAR array allows for the detection of cosmic rays in the energy range  $10^{16}$  –  $10^{18}$  eV.

Measurements of cosmic rays are performed mostly by using signals from LBAs. The LBAs are designed to operate between 10 MHz, where the ionospheric cut-off of radio wavelengths takes place, and 90 MHz where the commercial FM radio band starts. Nevertheless, due to the presence of strong Radio Frequency Interference (RFI) at the lowest frequencies, and the proximity of the FM band at the highest ones, the LBA operational range is limited between 30 – 80 MHz. Each LBA consists of two dipole arms oriented in the NE–SW and NW–SE direction.

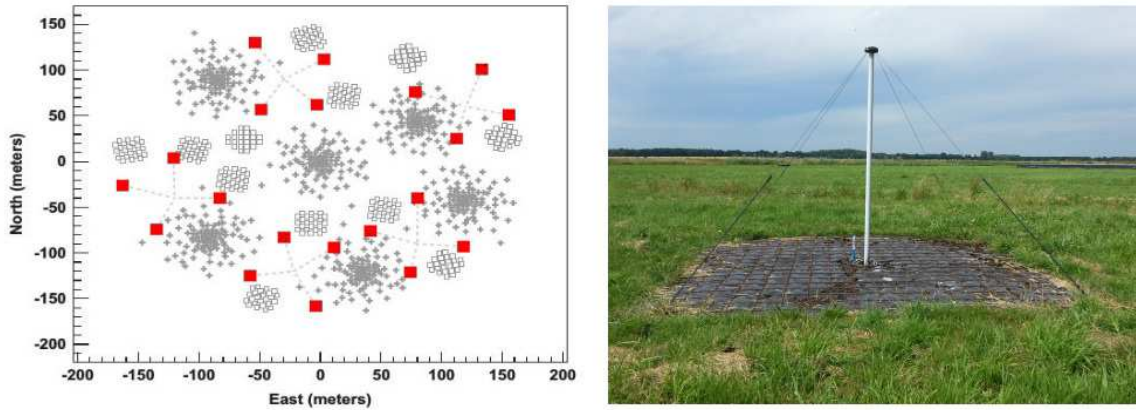


**Figure 1:** *Left:* layout of the six LOFAR central stations, the so-called *Superterp*. The location of LBA inner and outer antenna set is depicted as grey crosses; the position of the HBAs is shown as well (open grey squares). The red squares indicate the position of LORA scintillator detectors. *Right:* picture of one LBA.

### 3. Radio emission processes of extensive air showers

Secondary charged particles, produced in the atmosphere by the interaction of primary cosmic rays with the atmospheric nuclei, emit radio signals. Radio emission is generated by two mechanisms, the *geomagnetic* and the *charge excess process*. In the *geomagnetic process*, secondary electrons and positrons in the cascade are accelerated in opposite directions due to the Earth magnetic field. This effect creates a current which is linearly polarized in the direction perpendicular to the shower axis and to the geomagnetic field. In the *charge excess process* (also called *Askaryan effect* [13]), the radio emission is instead produced by a negative charge excess created at the shower front. In this latter case, the negative charge excess is caused by electrons which are knocked-out and start moving with the cascade, and by the annihilation of secondary positrons with electrons. The radiation emitted due to the *charge excess process* is polarized in the radial direction with respect to the shower axis. Thus, the combination of these two mechanisms creates an asymmetric distribution of the total radio signal around the shower axis [14, 15].

### 4. Analysis and results

In order to study a correlation between the radio frequency spectrum and EAS characteristics, the radio signal in the frequency-domain has been investigated on events detected by LOFAR since 2011. The analysis method used is the following:

- the signal intensity in the time-domain is converted into the frequency-domain by applying a Fast Fourier Transform (FFT). The FFT is calculated on a time-window of 128 samples (1 sample = 5 ns) corresponding to 640 ns time-window defined as  $[t_0 - 240 \text{ ns}, t_0 + 400 \text{ ns}]$  around the signal peak; the FFT squared module is then calculated (hereafter,  $|\text{FFT}|^2_{\text{signal}}$ )
- the background contribution is calculated on a longer time-window of  $2^{16}$  samples, equal to 328  $\mu\text{s}$ , centred on the pulse peak; this long time-window is divided in about 400 sub-

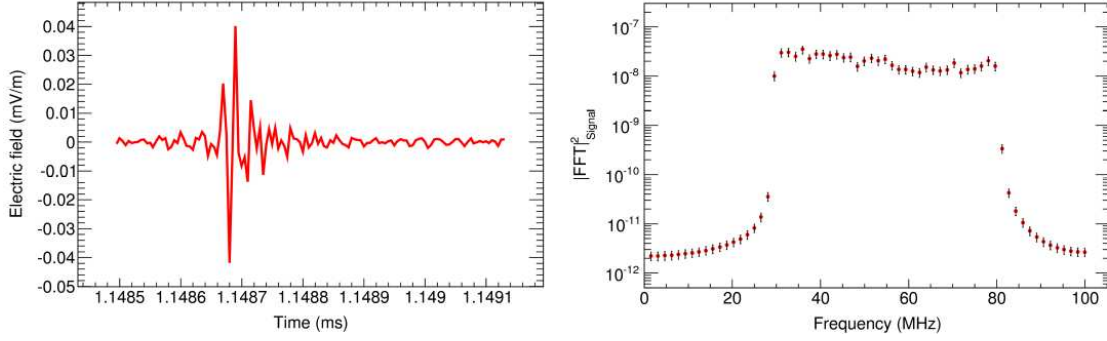


**Figure 2:** *Left:* electric field in the time-domain as measured by one LBA in the Superterp. The maximum intensity has a time length of about 50 ns, while the entire window is 640 ns long, and it is the one used in this analysis. *Right:* corresponding signal in the frequency-domain; the error bars on the  $|IFFT|^2$  correspond to an uncertainty of 20% which has been evaluated through a calibration analysis.

windows of 128 samples, after having excluded the pulse region. The  $|IFFT|^2_{\text{background}}$  is then calculated by averaging the  $|IFFT|^2$  on each of these sub-windows;

- the final  $|IFFT|^2$  is evaluated as  $|IFFT|^2 = |IFFT|^2_{\text{signal}} - |IFFT|^2_{\text{background}}$

Following the above method, the frequency spectrum has been characterised by fitting the  $\log_{10} |IFFT|^2$  with a linear function and looking for correlations between the slope of the linear fit and certain parameters. Figure 2 shows, for one event, the electric field measured by one antenna in the time-domain (*left*), and the corresponding signal in the frequency-domain (*right*) where the antenna band-filters at 30 MHz and 80 MHz are clearly visible. Errors on the  $|IFFT|^2$  have been evaluated from data taken during a calibration campaign performed in May 2014. The calibration measurements have been performed using an external emitting source positioned over one inner antenna of one Dutch station, and a difference of 20% in the receiving power between the two dipoles has been found. This uncertainty has been used as an error on the evaluation of the  $|IFFT|^2$  in this analysis (see figure 2–*right*). Figure 3–*left* shows the distribution of  $\log_{10} |IFFT|^2$  as function of frequency for one antenna of one event after the background subtraction. Due to the presence of many RFI around 30 MHz, which are removed during the data reduction process, most of the antennas displays a low radio signal intensity at 30 MHz. For this reason, the first point of the linear-fit region has been considered at 33 MHz. Furthermore, during this study, it has been observed that the frequency spectra measured in all antennas increase above 70 MHz. This is expected to be caused by the low-pass filter in the different antennas. Therefore, in order to not introduce any bias in the fitting procedure, the last point of the linear-fit region has been chosen at 70 MHz.

For each event, the linear-fit has been applied to all the antennas, in order to study the dependence of the slope parameter as function of distance to the shower axis. The antenna position at ground has been projected onto the plane perpendicular to the particle arrival direction vector  $\vec{v}$  (hereafter, *shower plane*). Since the linear-fit method is very sensitive to the signal-to-noise ratio detected in one shower event, strict selection criteria have been used in order to select good events for this analysis. Events have been selected by requiring that, at least in one station, half of the antennas show a pulse-peak value larger than  $10 \sigma$ , where  $\sigma$  is computed for each antenna in



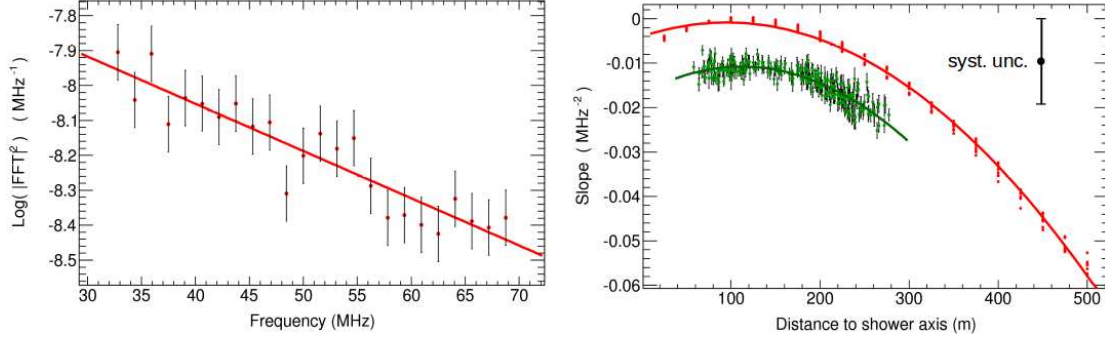


**Figure 3:** *Left:* distribution of  $\log_{10} |\text{FFT}|^2$  as function of frequency for one antenna of one detected event; the distribution has been fitted with a linear function, taking into account the 20% uncertainty on the  $|\text{FFT}|^2$  converted into logarithmic values. *Right:* distribution of the linear-fit slope as function of distance to the shower axis in the shower plane for one event (green points). The uncertainties on the slope values are obtained from the previous linear-fit procedure; the systematic uncertainties from the calibration procedures are shown on the top-right corner. Comparison with the corresponding simulated event is also shown (red points). Both distributions have been fitted with a parabolic function (solid line).

the long time-window of  $328 \mu\text{s}$ , as described previously. To these pre-selected events, for every frequency  $\nu$  in the range  $33 - 70 \text{ MHz}$ , the following criterion has been applied:

$$|\text{FFT}(\nu_i)|^2_{\text{Signal}} - |\text{FFT}(\nu_i)|^2_{\text{Background}} > \text{RMS} ( |\text{FFT}(\nu_i)|^2_{\text{Background}} ) \quad (4.1)$$

Events with less than 10 antennas satisfying condition 4.1 have been discarded. By using these selection criteria, 103 events have been selected and used for the analysis presented here. All the 103 selected events have been compared with the corresponding simulated events. CORSIKA simulations have been produced by using, as input, proton as primary particle, and energy and arrival direction as reconstructed from the real event. The antenna layout used in simulations (see figure 4) has been chosen in order to have a symmetric star-shape around the shower axis on the shower plane. Each simulated event has 160 antennas displayed at 25 m distance between each others on the shower plane, and distributed on 8 arms, thus covering an area of 500 m radius around the shower axis.

Figure 3—*right* shows the linear-fit slope as function of distance to the shower axis for one selected event (green points) together with one simulated event having the value of  $X_{\text{max}}$  closest to the observed one (red points). This event has a primary energy of  $(1.7 \pm 0.8) \cdot 10^{17} \text{ eV}$  as reconstructed by the LORA scintillator array, and a value of the atmospheric depth where the cascade reaches its maximum development  $X_{\text{max}} = (757 \pm 38) \text{ g/cm}^2$  as reconstructed by the radio Lateral Distribution Function (LDF) method [16]. The simulated event has  $X_{\text{max}} = 755 \text{ g/cm}^2$ .

As visible in figure 3—*right*, the distribution of the slope parameter as function of distance to the shower axis is well described by a parabolic function for both real data and simulations. The displayed error bars on the slope parameters have been extrapolated from the fitting procedure. Moreover, systematic uncertainties on the slope values (about  $0.01 \text{ MHz}^{-2}$ ) have been evaluated from the two antenna calibration procedures used at LOFAR [17], and are indicated on the top-right corner of the figure. Both distributions display a maximum at a distance around 100 m, in agree-

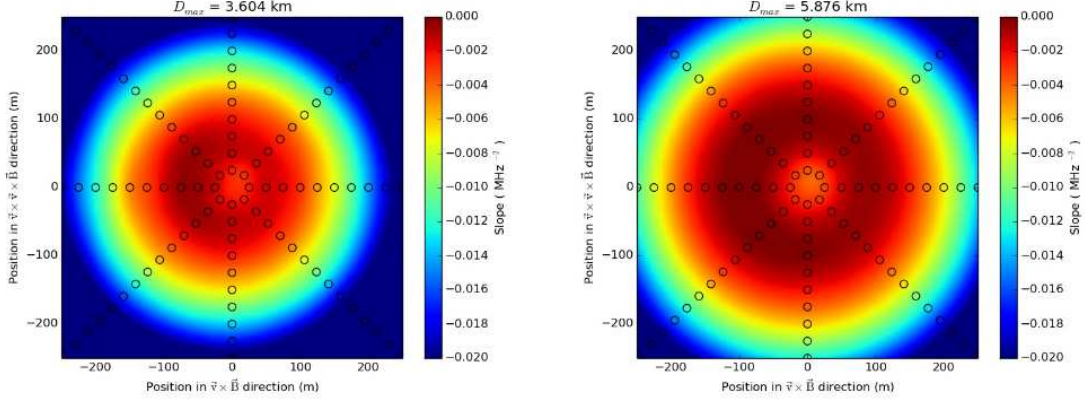


**Figure 4:** Distribution of the linear-fit slope on the shower plane for two simulated events with  $D_{\max} = 3.6$  km (*left*) and  $D_{\max} = 5.9$  km (*right*). In both figures values of the 160 antennas (open circles) have been interpolated in order to create a smooth background.

ment with the expectations from the *radio Cherenkov ring*, i.e. the region where the coherence of the radio signal is the uppermost. Nevertheless, the slope distribution for data shows a shift towards smaller slope values. Investigation of this shift is still on-going.

The analysis performed shows also that the slope parameter depends on the geometrical distance of the observer from  $X_{\max}$  (hereafter  $D_{\max}$ ). Figure 4 shows the distribution of the slope parameter on the shower plane for two simulated events having a value of  $D_{\max} = 3.6$  km (*left*) and  $D_{\max} = 5.9$  km (*right*) respectively. For all the 103 selected events, the linear-fit procedure has been applied, and only events with a good parabolic fit of the slope parameter as function of distance to the shower axis have been considered. Figure 5 shows the distribution of the slope parameter as function of  $D_{\max}$  at 180 m and 220 m distance from the shower axis (blue points). The distributions have been fitted with the following function:

$$\text{slope}(D_{\max}) = \frac{\alpha}{1 + \exp(-\beta \cdot D_{\max})} - \gamma \quad (4.2)$$

This fit-function has been previously used on AERA data as described in [11], and has been adjusted to LOFAR data by adding a third free parameter. This was needed because of the different geographical location and different antenna design. Distributions shown in figure 5 display a good agreement between the data points and the fit-function, even if the reliability of the fit is affected by the large uncertainties on  $D_{\max}$  (about 300 m). A full parametrization of the frequency spectrum as function of  $D_{\max}$  is still under investigation.

## 5. Conclusions and outlook

The radio frequency spectrum in the 30 – 70 MHz range has been studied. The analysis has been conducted on cosmic ray radio signals detected by LOFAR and on the corresponding simulated events. Results show a clear dependence of the frequency spectrum on the distance to the



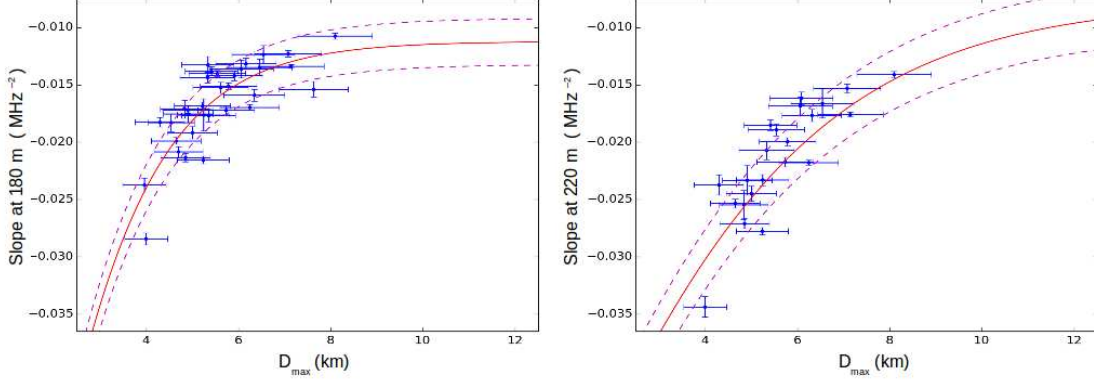


**Figure 5:** Distribution of the linear-fit slope parameter as function of  $D_{\max}$  at 180 m (*left*) and 220 m (*right*). Uncertainties on the slope parameter have been extrapolated from the linear-fit procedure. Uncertainties on  $D_{\max}$  have been evaluated from  $\sigma_{X_{\max}} = 38 \text{ g/cm}^2$  [16]. The red lines indicate the result of the fit obtained using equation 4.2, with the 68% confidence region delimited by the dashed purple lines.

shower axis, as predicted by theoretical and analytical calculations. However, the obtained spectral indices for real data are systematically steeper than for simulated showers. This discrepancy is currently under investigation. These characteristics of radio signals can be used as an additional independent method to reconstruct the position of the shower axis at ground. Studies about this option are on-going [18].

Furthermore, a dependence of the frequency spectrum on the geometrical distance to the shower maximum  $D_{\max}$  has been investigated. Results show that, at a fix distance from the shower axis, the slope parameter of the frequency spectrum increases as  $D_{\max}$  increases. This is related to the fact that the majority of the radio emission is emitted at an height around  $X_{\max}$ , and then propagates with an opening angle of  $\sim 1^\circ$  given by the atmosphere refractive index. Thus, if the primary interaction happens at higher altitude, the radio footprint is projected from a higher altitude on a larger surface. A study on how to use the frequency spectrum as an independent method to reconstruct  $X_{\max}$  for events detected by LOFAR is still on-going.

## Acknowledgments

The LOFAR cosmic ray key science project acknowledges funding from an Advanced Grant of the European Research Council (FP/2007-2013) / ERC Grant Agreement n. 227610. The project has also received funding from the European Research Council (ERC) under the European Union's Horizon 2020 research and innovation programme (grant agreement No 640130). We furthermore acknowledge financial support from FOM, (FOM-project 12PR3041-3) and NWO (Top Grant 614-001-454, and Spinoza Prize SPI 78-409). AN is supported by the DFG (research fellowship NE 2031/1-1).

LOFAR, the Low Frequency Array designed and constructed by ASTRON, has facilities in several countries, that are owned by various parties (each with their own funding sources), and that

are collectively operated by the International LOFAR Telescope foundation under a joint scientific policy.

## References

- [1] J.V. Jelley et al., *Radio pulses from extensive cosmic-ray air showers*, *Nature* **205** (1965) 327–328
- [2] D. Ardouin et al., *Radio-detection signature of high-energy cosmic rays by the CODALEMA experiment*, *Nucl. Instr. Meth. Phys. Res., A* **555** (2005) 148–163 [[astro-ph/0504297](#)]
- [3] H. Falcke et al. *Detection and imaging of atmospheric radio flashes from cosmic ray air showers*, *Nature* **435** (2005) 313–316
- [4] M.P. van Haarlem et al., *LOFAR: The Low-Frequency ARray*, *A&A* **556** A2 (2013) 53 [[astro-ph.IM/1305.3550](#)]
- [5] A. Aab et al., *The Pierre Auger Cosmic Ray Observatory*, *Nucl. Instr. Meth. Phys. Res., A* **798** (2015) 172–213 [[astro-ph.IM/1502.01323](#)]
- [6] P.A. Bezyazeev et al. *Measurement of cosmic-ray air showers with the Tunka Radio Extension (Tunka-Rex)*, *NIM, A* **802** (2015) 89–96 [[astro-ph.IM/1509.08624](#)]
- [7] H.R. Allan, *Radio Emission From Extensive Air Showers*, *Prog. in Element. Part. and Cos. Ray Phys.* **10** (1971) 171–302
- [8] H. Falcke and P.W. Gorham, *Detecting Radio Emission from Cosmic Ray Air Showers and Neutrinos with a Digital Radio Telescope*, *Astroparticle Physics* **19** (2003) 477–494
- [9] T. Huege and H. Falcke, *Radio-Emission from Cosmic Ray Air Showers: Coherent Geosynchrotron Radiation*, *A&A* **412** (2003) 19–34
- [10] T. Huege and H. Falcke, *Radio emission from cosmic ray air showers. Monte Carlo simulations*, *A&A* **430** (2005) 779–798
- [11] S. Jansen, *PhD thesis, Radio for the Masses - Cosmic ray mass composition measurements in the radio frequency domain* (2016) ISBN 978 94 028 0073 9
- [12] S. Thoudam et al., *LORA: A scintillator array for LOFAR to measure extensive air shower*, *Nucl. Instr. Meth. Phys. Res. A* **767** (2014) 339 [[physics.ins-det/1408.4469](#)]
- [13] G.A. Askaryan, *Excess Negative Charge of an Electron-Photon Shower and its Coherent Radio Emission*, *JETP*, **14** (1962) 441–443
- [14] O. Scholten, K. Werner, and F. Rusydi, *A macroscopic description of coherent geo-magnetic radiation from cosmic-ray air showers*, *Astroparticle Physics* **29**: 94–103, 2008 [[astro-ph/0709.2872](#)]
- [15] K. Werner and O. Scholten, *Macroscopic Treatment of Radio Emission from Cosmic Ray Air Showers based on Shower Simulations*, *Astroparticle Physics* **29** (2008) 393–411 [[astro-ph/0712.2517](#)]
- [16] A. Nelles et al., *The radio emission pattern of air showers as measured with LOFAR – a tool for the reconstruction of energy and shower maximum*, *JCAP* **05** (2015) 18 [[astro-ph.HE/1411.7868](#)]
- [17] A. Nelles et al., *Calibrating the absolute amplitude scale for air showers measured at LOFAR*, *JINST* **10** (2015) P11005 [[astro-ph.IM/1507.08932](#)]
- [18] A. Bonardi et al., *Study of the LOFAR self-trigger and single-station acquisition mode*, in proceedings of 35<sup>th</sup> ICRC, *PoS (ICRC2017)* 402 (2017)

# The effect of the atmospheric refractive index on the radio signal of extensive air showers using Global Data Assimilation System (GDAS)

---

**A. Corstanje<sup>2</sup>, P. Mitra<sup>1\*</sup>, A. Bonardi<sup>2</sup>, S. Buitink<sup>1</sup>, H. Falcke<sup>2,3,4</sup>, B. M. Hare<sup>5</sup>, J.R. Hörandel<sup>2,3</sup>, K. Mulrey<sup>1</sup>, A. Nelles<sup>2,6</sup>, J.P. Rachen<sup>2</sup>, L. Rossetto<sup>2</sup>, P. Schellart<sup>2,8</sup>, O. Scholten<sup>5,7</sup>, S. ter Veen<sup>2,4</sup>, S. Thoudam<sup>2,9</sup>, T.N.G. Trinh<sup>5</sup>, T. Winchen<sup>1</sup>**

<sup>1</sup> *Astrophysical Institute, Vrije Universiteit Brussel, Pleinlaan 2, 1050 Brussels, Belgium*

<sup>2</sup> *Department of Astrophysics / IMAPP, Radboud University Nijmegen, P.O. Box 9010, 6500 GL, Nijmegen, The Netherlands*

<sup>3</sup> *NIKHEF, Science Park Amsterdam, 1098 XG Amsterdam, The Netherlands*

<sup>4</sup> *Netherlands Institute of Radio Astronomy (ASTRON), Postbus 2, 7990 AA Dwingeloo, The Netherlands*

<sup>5</sup> *KVI-CART, University Groningen, P.O. Box 72, 9700 AB Groningen, The Netherlands*

<sup>6</sup> *Department of Physics and Astronomy, University of California Irvine, Irvine, CA 92697-4575, USA*

<sup>7</sup> *Interuniversity Institute for High-Energy, Vrije Universiteit Brussel, Pleinlaan 2, 1050 Brussels, Belgium*

<sup>8</sup> *Department of Astrophysical Sciences, Princeton University, Princeton, NJ 08544, USA*

<sup>9</sup> *Department of Physics and Electrical Engineering, Linnéuniversitetet, 35195 Växjö, Sweden*  
E-mail: [pragati.mitra@vub.ac.be](mailto:pragati.mitra@vub.ac.be)

One of the major systematic uncertainties in the measurement of  $X_{\max}$  from radio emission of EAS arises from variations of the refractive index in the atmosphere. The refractive index  $n$  varies with temperature, humidity and pressure, and the variations can be on the order of 10% for  $(n-1)$  at a given altitude. The effect of a varying refractive index on  $X_{\max}$  measurements is evaluated using CoREAS: a microscopic simulation of the radio emission from the individual particles in the cascade simulated with CORSIKA. We discuss the resulting offsets in  $X_{\max}$  for different frequency regimes, and compare them to a simple physical model. Under typical circumstances, the offsets in  $X_{\max}$  range from 4-11 g/cm<sup>2</sup> for the 30-80 MHz frequency band. Therefore, for precise measurements it is required to include atmospheric data at the time and place of observation of the air shower into the simulations. The aim is to implement this in the next version of CoREAS/CORSIKA using the Global Data Assimilation System (GDAS), a global atmospheric model based on meteorological measurements and numerical weather predictions. This can then be used to re-evaluate the air shower measurements of the LOFAR radio telescope.

*35th International Cosmic Ray Conference ICRC217-  
10-20 July, 2017  
Bexco, Busan, Korea*

---

\*Speaker.

## 1. Introduction

In recent years, the field of radio detection of high-energy air showers has advanced quite rapidly. Estimating the depth of shower maximum  $X_{\max}$  with improved accuracy is of great interest for the study of primary particle composition [1]. The highest precision to the determination of  $X_{\max}$  with radio technique is currently achieved with the LOFAR radio telescope, situated in the north of the Netherlands. The central ring of LOFAR consists of 288 low-band antennas within the diameter of 320 meters, recording cosmic ray events within 30-80 MHz. Additionally, there are also 288 high-band antennas measuring in the 110-190 MHz range [2]. The densely instrumented core of LOFAR gives the opportunity to investigate the radio footprint i.e. the lateral intensity distribution in close detail and enables to infer  $X_{\max}$  to a precision of 20 g/cm<sup>2</sup> which is comparable to the precision achieved in fluorescence detectors [3].

The measured lateral intensity distributions are compared to CoREAS [4], a simulation package of the radio emission from the individual particles in the cascade simulated with CORSIKA [5]. The detected radio signal depends on the difference in travel times of radio waves and particles. Therefore, it is important to apply an accurate value of the refractive index  $n$ . Variations in the refractive index lead to changes in the radio intensity footprint on the ground because the angle of peak emission depends on  $n$  [6]. In CORSIKA, the standard US atmosphere is used as the default model atmosphere featuring constant temperature lapse with altitude and zero humidity. Thus a realistic model calls for more accurate description of atmosphere.

The Global Data Assimilation System (GDAS) developed at NOAA's National Centers for Environmental Prediction (NCEP) is a tool to study realistic atmosphere [7]. It is run four times a day (0, 6, 12, and 18 UTC) and provides a 3-, 6- and 9-hour forecast based on the interpolation of the meteorological measurements from all over the world including weather stations on land, ships, and airplanes as well as radiosondes and weather satellites. The three hourly data are available at 23 constant pressure levels, from 1000 hPa (roughly sea level) to 20 hPa ( $\approx 26$  km) on a global 1° spaced latitude-longitude grid (180° by 360°). Each data set is complemented by data for the surface level. The data are stored in weekly files and made available online.

## 2. Analysis and results

The effect of refractivity on the radio footprint can be better comprehended from a simple toy model as depicted on the left panel of **Fig 1**. Because of propagation effects, the radio pulse is compressed, depending on the viewing angle. The compression is maximal at the Cherenkov angle where the emission is thus coherent up to much higher frequencies. Roughly above 100 MHz, the emission strongly peaks at the Cherenkov angle, forming a ring of radiation on the ground [8]. Below 100 MHz, the radiation pattern has a more complicated structure, but its size still scales with the Cherenkov angle. The relation between  $n$  and Cherenkov angle  $\alpha$  is given by

$$\cos \alpha = \frac{1}{\beta n(h)}. \quad (2.1)$$

The model is based on the assumption that most of the radiation is produced near  $X_{\max}$  and the size of the footprint scales with distance to  $X_{\max}$  and with the Cherenkov angle at that distance. if the

refractive index is higher than expected, the Cherenkov angle becomes larger. The measured size of the radiation footprint now corresponds to a lower emission altitude, and therefore a larger  $X_{\max}$ . Using CoREAS simulations we have also determined the systematic offset in  $X_{\max}$  measurement for a 10% increase in refractivity. Two ensembles of showers are compared, by taking one shower from the ensemble of higher refractivity and fitting the lateral intensity distribution by all 50 from normal refractivity ensemble. A mean squared error is used as a fit quality measure. For every shower, fit quality is plotted against  $X_{\max}$  showing a minimum with a quadratic dependence and therefore fitted to a parabola. The location of the minimum of the parabola is used as an estimator for  $X_{\max}$ . An typical example is shown on the right panel of **Fig 1**. The average between the difference of the newly fitted and true  $X_{\max}$  yields the systematic offset in  $X_{\max}$ . Details of this analysis can be found in [6]. With a linear fit to the points the offsets found are nearly half of that obtained from Cherenkov toy model described above between 30-80 MHz as shown in **Fig 2**. This indicates that Cherenkov time compression is not the only determining factor behind the shape of the radio footprint. The offset ranges from 9 g/cm<sup>2</sup> for 15° zenith to 18 g/cm<sup>2</sup> for 45° zenith. The relation for the offset  $\Delta X$  as a function of distance to  $X_{\max}$  ( $R$ ) for 10% higher refractivity is given as

$$\Delta X_{10\%} = 3 \frac{R}{1 \text{ km}} - 1.37 \text{ g/cm}^2. \quad (2.2)$$

and for higher frequencies the difference in offset between simulation and Cherenkov model decreases because the the toy model more accurately describes the radiation pattern [6]. In order to

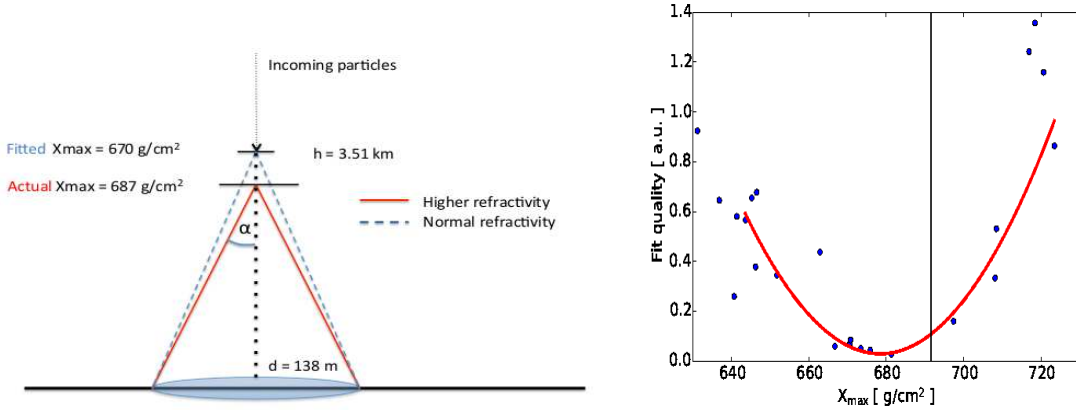


**Figure 1:** **Left**— Sketch of Cherenkov model: the effect of an increase in  $n$  is shown schematically, for a proton primary particle of  $10^{17}$  eV from zenith having an average  $X_{\max} = 670 \text{ g/cm}^2$  as obtained from CoREAS simulations, corresponding to an altitude of 3.51 km. 10% higher refractivity than the default value used in CoREAS ( $N = 292$  at sea level), results in a higher  $X_{\max}$  (red line), than the normal one (blue line). The modeled difference in  $X_{\max}$  amounts to 17 g/cm<sup>2</sup> [6]. **Right**— Fit quality as a function of  $X_{\max}$ . The simulated  $X_{\max}$  for the shower with higher refractivity is indicated by the black vertical line. The minimum gives the best fit value. The scatter around the minimum arises due to shower to shower fluctuation.

model a realistic atmosphere one needs to obtain the suitable atmospheric parameters from GDAS. Parameters like temperature, relative humidity and pressure can be directly extracted from GDAS files. Other parameters can be calculated using physical relations involving those first three pa-

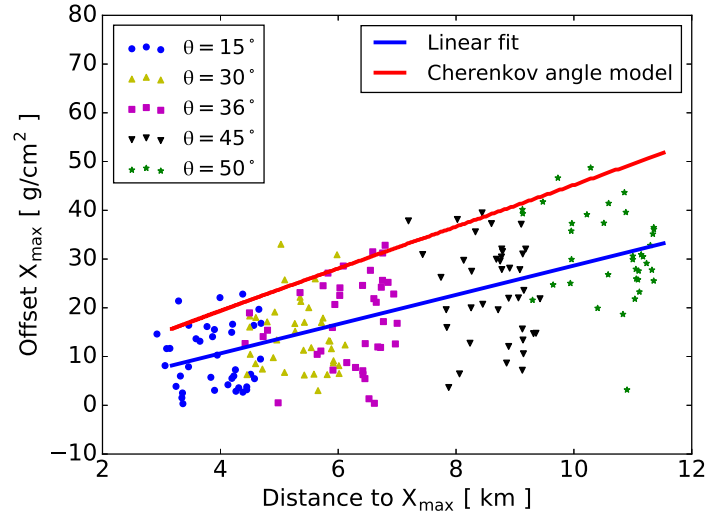


**Figure 2:**  $X_{\max}$  offset for different zenith angles for LOFAR low band frequency range (30 – 80 MHz), where the points represent individual simulated shower. The blue line is a linear fit to the data and the red line is from the Cherenkov model [6].

rameters. To calculate the air density, the relative humidity must be converted into water vapor pressure, the partial pressure of water in air in hPa. This conversion depends on air temperature. The following approximation of the empirical Magnus formula is used in the calculations [9]:

$$e = \frac{h}{100\%} \times 6.1070 \times \exp\left(\frac{21.88 t}{265.5 + t}\right) \quad \text{for } t \geq 0^\circ\text{C} \quad (2.3)$$

and

$$e = \frac{h}{100\%} \times 6.1070 \times \exp\left(\frac{17.15 t}{234.9 + t}\right) \quad \text{for } t \leq 0^\circ\text{C} \quad (2.4)$$

The density in can be calculated from ideal gas equation as

$$\rho = \frac{P M_{\text{air}}}{R T} \quad (2.5)$$

where  $P$ ,  $T$  and  $R$  are pressure, temperature, universal gas constant respectively and  $M_{\text{air}}$  is the molar mass of air which can be calculated from the contributions of dry air, water vapor and  $\text{CO}_2$ . Next, the refractivity  $N$  as a function of humidity, pressure and temperature can be expressed as

$$N = 77.6890 \frac{p_d}{T} + 71.2952 \frac{p_w}{T} + 375463 \frac{p_w}{T^2} \quad (2.6)$$

with  $p_w$ ,  $p_d$  and  $T$  being the partial water vapor pressure (hPa), partial dry air pressure (hPa) and temperature respectively. In the regime of radio frequency higher value of humidity increases the refractivity. On the right panel of **Fig 3** it is shown that the day to day humidity has a huge variance. It is thus necessary to use the detailed atmospheric conditions at the time of observation.

In order to incorporate atmospheric parameters extracted from GDAS to CORSIKA/CoREAS



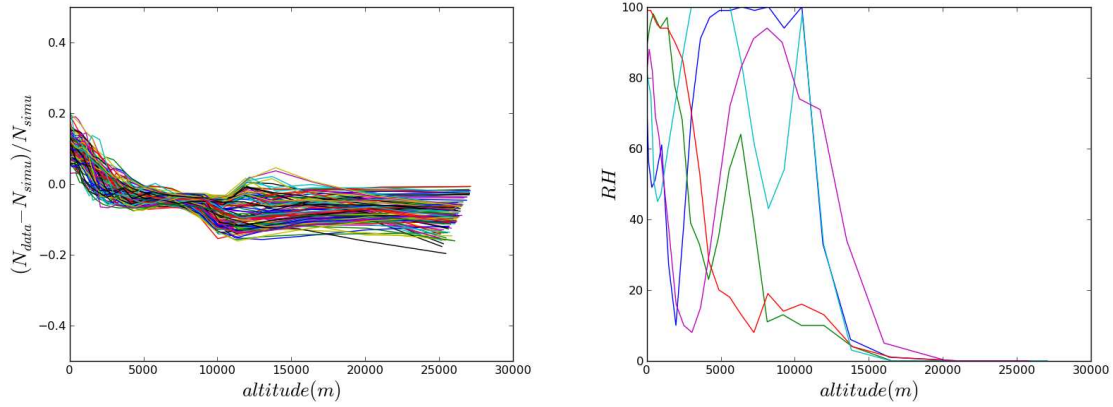


**Figure 3:** **Left**— The relative refractivity plot as a function of altitude for different times over 3 years for 100 cosmic ray events recorded at Lofar. Relative refractivity is defined as the ratio of difference between data and simulation to data. It fluctuates from approximately 20% above default value to 10% below the default value used in CoREAS between 0-5 km of altitude. This variation is indeed is the effect of rapidly varying temperature and humidity between the above mentioned altitude range. Also between 3-8 km the relative variation in refractivity is about 3% – 5%. This altitude range is of interest as this is usually where the shower reaches its maximum. **Right**— Relative humidity plot as a function of altitude for 5 random events. It changes quite rapidly over the altitude and becomes negligible after around 12 km as this marks the end of troposphere.

we have developed a script that will download the required GDAS file given the time and location of observation of the event and return values of refractive index between ground and highest GDAS level within 1m interval. It also fits the density profile according to the standard 5 layered atmospheric model used in CORSIKA[5]. In this model the density  $\rho(h)$  follows an exponential dependence on the altitude leading to the functional form of mass overburden  $T(h)$  which is the density integrated over height as

$$T(h) = a_i + b_i \cdot e^{-h/c_i} \quad i = 1, \dots, 4 \quad (2.7)$$

Thus the density

$$\rho(h) = b_i/c_i \cdot e^{-h/c_i} \quad i = 1, \dots, 4 \quad (2.8)$$

In the fifth layer the overburden is assumed to decrease linearly with height. The parameters  $a_i$ ,  $b_i$  and  $c_i$  are to be obtained in a manner that the function  $T(h)$  is continuous at the layer boundaries and can be differentiated continuously. We distribute 24 GDAS density points into 3 layers with the layers having boundaries approximately around 4 km for first layer, 9.5 km for second layer and between 26-28 km for the third layer. A point to note here is that the layer boundaries are not constant but rather can change slightly depending on the place of observations and time. Next, we fit the data to Eq 2.8 in the following way-

For layer 1 we fit the density profile with two free parameters. Then we calculate density  $\rho_1$  at boundary 1 from Eq 2.8 using the obtained parameters  $b_1$ ,  $c_1$ . The boundary condition that the density has to be continuous at the boundaries reduces the number of free parameters to 1 and the

parameter  $b_2$  for second layer can be expressed as a function of  $\rho_1$  and  $c_2$  with  $c_2$  being the only free parameter. Similarly we continue the same procedure for the higher layers. Since now we have the smooth profile for density we can analytically solve for the parameter  $a$  in Eq 2.7 exploiting the boundary conditions for mass overburden. The parameterization for fifth layer is adapted from the US standard atmosphere [5]. An example of the fit is shown in Fig 4.

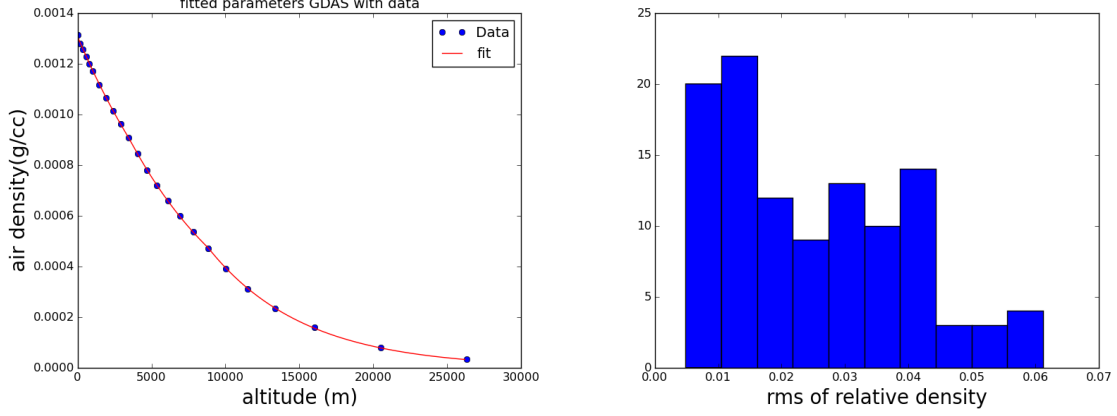


**Figure 4:** **Left**— density vs altitude profile for an arbitrary event, blue dots are GDAS data points and the red line is the fitted profile using the CORSIKA parameterization. **Right**—Histogram for rms value of relative density for 100 different events. The relative density is defined as  $\frac{\rho_{fit} - \rho_{data}}{\rho_{fit}}$ . The small value indicates the good quality of fit though a small bias towards positive values is introduced probably because of the imposed boundary conditions.

### 3. Conclusion and outlook

For mass composition analysis the accuracy of the  $X_{max}$  measurement is crucial. For  $X_{max}$  measurements with the radio technique we have investigated the systematic error due to variations in the atmospheric refractive index in particular for LOFAR measurements; for higher refractivity the offsets are found to be proportional to the distance to  $X_{max}$  for different zenith angles. We also have proposed a toy model based on the Cherenkov emission at  $X_{max}$  altitude that qualitatively describes this effect especially for higher frequency range (120-250 MHz). Given variations in  $N$  on the order of 4%, from the atmospheric effects the offsets would range from about 3.5-11 g/cm<sup>2</sup> for 30-80 MHz, although one can not use a single value of refractivity in simulation as it does not provide full information of realistic atmosphere. Using GDAS we studied the local atmospheric profiles for refractivity and humidity at the time of several cosmic ray events recorded at LOFAR. The parameters show significant variations over time. The relative variation in refractivity is found to be around 3% – 5% between 3-8 km of altitude. We have implemented GDAS atmospheric profiles with local refractive index lookup table and improved density parametrization to COREAS/CORSIKA. These modifications will be included in a future release of CORSIKA/CoREAS together with a standalone script that downloads GDAS files and produces atmosphere profiles and CORSIKA steering files. The script is flexible and is able to create profiles for any location on Earth. However, for very specialized applications, such as near-horizontal showers,



further development will be needed. Also current work is going on the re-evaluation of LOFAR measurements with improved atmosphere.

#### 4. Acknowledgement

The LOFAR cosmic ray key science project acknowledges funding from an Advanced Grant of the European Research Council (FP/2007-2013) / ERC Grant Agreement no 227610. The project has also received funding from the European Research Council (ERC) under the European Union's Horizon 2020 research and innovation program (grant agreement No 640130). We furthermore acknowledge financial support from FOM, (FOM-project 12PR304) and NWO (VENI grant 639-041-130). AN is supported by the DFG (research fellowship NE 2031/1-1). LOFAR, the Low Frequency Array designed and constructed by ASTRON, has facilities in several countries, that are owned by various parties (each with their own funding sources), and that are collectively operated by the International LOFAR Telescope foundation under a joint scientific policy.

#### References

- [1] S. Buitink et al. A large light-mass component of cosmic rays at  $10^{17} - 10^{17.5}$  eV from radio observations. *Nature*, 531:70, 2016.
- [2] P. Schellart et al. Detecting cosmic rays with the LOFAR radio telescope. *Astronomy and Astrophysics*, 560(A98), 2013.
- [3] S. Buitink et al. Method for high precision reconstruction of air shower  $X_{\text{max}}$  using two-dimensional radio intensity profiles. *Phys. Rev. D*, 90(8), 2014.
- [4] Tim Huege and Clancy W. James. Full Monte Carlo simulations of radio emission from extensive air showers with CoREAS. In *Proceedings, 33rd International Cosmic Ray Conference (ICRC2013): Rio de Janeiro, Brazil, July 2-9, 2013*, page 0548, 2013.
- [5] D. Heck et al. CORSIKA: A Monte Carlo code to simulate extensive air showers. *Report FZKA*, 6019, 1998.
- [6] A. Corstanje et al. The effect of the atmospheric refractive index on the radio signal of extensive air showers. *Astropart. Phys.*, 89:23–29, 2017.
- [7] National oceanic and atmospheric administration, global data assimilation system.
- [8] A. Nelles et al. Measuring a Cherenkov ring in the radio emission from air showers at 110–190 MHz with LOFAR. *Astropart. Phys.*, 65:11–21, 2015.
- [9] P. Abreu et al. Description of Atmospheric Conditions at the Pierre Auger Observatory using the Global Data Assimilation System (GDAS). *Astropart. Phys.*, 35:591–607, 2012.



# Circular polarization in radio emission from extensive air showers

---

**Olaf Scholten<sup>\*1,2</sup>, T.N.G. Trinh<sup>1</sup>, A. Bonardi<sup>3</sup>, S. Buitink<sup>4</sup>, A. Corstanje<sup>3</sup>, H. Falcke<sup>3,5,6</sup>, B.M. Hare<sup>1</sup>, J.R. Hörandel<sup>3,5</sup>, P. Mitra<sup>4</sup>, K. Mulrey<sup>4</sup>, A. Nelles<sup>3,7</sup>, J.P. Rachen<sup>3</sup>, L. Rossetto<sup>3</sup>, P. Schellart<sup>3,9</sup>, S. ter Veen<sup>3,7</sup>, S. Thoudam<sup>3,8</sup>, T. Winchen<sup>4</sup>**

<sup>1</sup> *University of Groningen, KVI Center for Advanced Radiation Technology, 9747 AA Groningen, The Netherlands*

<sup>2</sup> *Interuniversity Institute for High-Energy, Vrije Universiteit Brussel, Pleinlaan 2, 1050 Brussels, Belgium*

<sup>3</sup> *Department of Astrophysics/IMAPP, Radboud University, P.O. Box 9010, 6500 GL Nijmegen, The Netherlands*

<sup>4</sup> *Astrophysical Institute, Vrije Universiteit Brussel, Pleinlaan 2, 1050 Brussels, Belgium*

<sup>5</sup> *Nikhef, Science Park Amsterdam, 1098 XG Amsterdam, The Netherlands*

<sup>6</sup> *Netherlands Institute for Radio Astronomy (ASTRON), 7990 AA Dwingeloo, The Netherlands*

<sup>7</sup> *Department of Physics and Astronomy, University of California, Irvine, CA 92697-4575, USA*

<sup>8</sup> *Department of Physics and Electrical Engineering, Linnéuniversitetet, 35195 Växjö, Sweden*

<sup>9</sup> *Department of Astrophysical Sciences, Princeton University, Princeton, NJ 08544, USA*

*E-mail: [Scholten@KVI.nl](mailto:Scholten@KVI.nl)*

At LOFAR we measure the radio emission from extensive air showers (EAS) in the frequency band of 30 – 80 MHz in dual-polarized antennas. Through an accurate antenna calibration we can determine the complete set of four Stokes parameters that uniquely determine the linear and circular polarization of the radio signal for an EAS. The observed dependency of the circular polarization on azimuth angle and distance to the shower axis is explained as due to the interfering contributions from the two different radiation mechanisms, a main contribution due to a geomagnetically-induced transverse current and a secondary component due to the Askaryan effect. The measured data show a quantitative agreement with microscopic CORSIKA/CoREAS calculations. Having a very detailed understanding of radio emission from EAS, opens the possibility to use circular polarization as an investigative tool in the analysis of air shower structure, such as for the determination of atmospheric electric fields.

*35th International Cosmic Ray Conference — ICRC2017  
10–20 July, 2017  
Bexco, Busan, Korea*

---

<sup>\*</sup>Speaker.

## 1. Introduction

The understanding of the mechanism of radio emission from extensive air showers (EAS) has reached a level that makes this process suitable for high-precision studies. As a prime example we treat in this contribution the circular polarization of the radiation. As we will show, this is due to a rather subtle interference of the two main emission mechanisms, geomagnetic and charge excess radiation. Because of this high level of understanding of the emission mechanism the radio emission from EAS induced by energetic cosmic rays is a very sensitive way to determine shower properties, such as energy [1, 2] and  $X_{\max}$ , the atmospheric (slant) depth where the number of air-shower particles reaches a maximum [3, 4]. The latter is a measure of the mass composition of the primary cosmic rays [5, 6].

Microscopic models based on first principles have been developed to calculate the radio emission from the EAS such as CoREAS [7] and ZHAireS [8]. Their predictions agree to a high level of precision with measurements at LOFAR (LOw-Frequency ARray) [9, 10] and other radio antenna arrays [11], see also Ref. [4].

To get insight in the coherent radiation mechanisms a macroscopic view of the shower is essential. The Lorentz force,  $\hat{e}_{\vec{v} \times \vec{B}} \propto \hat{e}_{\vec{v}} \times \hat{e}_{\vec{B}}$ , induces a current in the plasma cloud at the shower front that is transverse to the shower direction which is given by  $\hat{e}_{\vec{v}}$ .  $\hat{e}_{\vec{B}}$  denotes the direction of the geomagnetic field. A secondary contribution [12], due to the net negative charge in the plasma cloud, is also known as Askaryan radiation [13]. The associated current is parallel to  $\hat{e}_{\vec{v}}$ . In the far-field regime radiation is polarized in the plane spanned by the emitting current and the observer while it is perpendicular to its propagation direction. We thus obtain that the geomagnetic component is polarized in the  $\hat{e}_{\vec{v} \times \vec{B}}$  direction while radial for charge-excess radiation. This is also confirmed by observations [14, 15, 16, 17, 18].

The radio pulse has also a certain amount of circular polarization [19]. As has recently been shown [20] the circular polarization is caused by a slight, of order 1 ns, time-shift between the pulses emitted by the two emission mechanisms due to a different dependence on the viewing angle to the shower axis [12, 21]. The circular polarization thus constitutes an accurate test of the differences between the geomagnetic and the charge excess emission mechanisms. At LOFAR we have measured the Stokes parameters [17] for radio emission and shown that these are a convenient way to express the complete polarization of the radio pulse. The data are in excellent agreement with the model calculations.

## 2. LOFAR

LOFAR [22] is a digital radio telescope where for the present measurements we use only the Low Band Antennas (LBAs), each consisting of two inverted V-shaped dipoles where we used the 30 - 80 MHz band. We usually store 2.1 ms of data, sampled at 200 Msamples/s per antenna after a trigger from the LORA scintillator array. Using the reconstructed arrival direction, the polarization directions of the signal are chosen in the direction of the Lorentz force  $\hat{e}_{\vec{v} \times \vec{B}}$  and  $\hat{e}_{\vec{v} \times \vec{v} \times \vec{B}}$ . The instrumental influences induced by the antenna and the amplifier are corrected for in this process. For the present analysis the antenna positions are projected onto the shower plane which is defined as the plane perpendicular to the shower,  $\hat{e}_{\vec{v}}$ , and going through the core of the shower on the

ground. A detailed description of the offline analysis of the data for cosmic ray science can be found in [9, 3, 17].

The Stokes parameters are most easily expressed in terms of the complex voltages  $\mathcal{E}_i = E_i + i\hat{E}_i$ ,

$$\begin{aligned} I &= \frac{1}{n} \sum_0^{n-1} \left( |\mathcal{E}_{i, \vec{v} \times \vec{B}}|^2 + |\mathcal{E}_{i, \vec{v} \times \vec{v} \times \vec{B}}|^2 \right) \\ Q &= \frac{1}{n} \sum_0^{n-1} \left( |\mathcal{E}_{i, \vec{v} \times \vec{B}}|^2 - |\mathcal{E}_{i, \vec{v} \times \vec{v} \times \vec{B}}|^2 \right) \\ U + iV &= \frac{2}{n} \sum_0^{n-1} \left( \mathcal{E}_{i, \vec{v} \times \vec{B}} \mathcal{E}_{i, \vec{v} \times \vec{v} \times \vec{B}}^* \right), \end{aligned} \quad (2.1)$$

Here  $E_i$  is sample  $i$  of the electric field component in either the  $\hat{e}_{\vec{v} \times \vec{B}}$  or the  $\hat{e}_{\vec{v} \times \vec{v} \times \vec{B}}$  polarization direction and  $\hat{E}_i$  its Hilbert transform [17]. For the present analysis the summations are performed over  $n = 5$  samples, of 5 ns each, centered around the pulse maximum. The linear-polarization direction makes an angle  $\psi = \frac{1}{2} \tan^{-1}(U/Q)$  with the  $\vec{v} \times \vec{B}$ -axis. The circular polarization is given by  $V/I$ . It is convenient to define  $W^2 = I^2 - (Q^2 + U^2 + V^2)$  which is a measure of the difference in structure of the signal in the two polarization directions, likely due to noise, see Ref. [20] for a more extensive discussion.

### 3. Interpretation

Circular polarization can be understood as the rotation of the polarization direction over the duration of the pulse, due to a time lag between the charge excess and geomagnetic pulses. To quantify this it is conceptually easiest to consider a signal of fixed frequency  $\omega$ . The radially-polarized charge-excess pulse,

$$\mathcal{E}_C(t) = E_C e^{i\omega(t-\Delta t)} (\cos \phi \hat{e}_{\vec{v} \times \vec{B}} + \sin \phi \hat{e}_{\vec{v} \times \vec{v} \times \vec{B}}),$$

thus has a time lag of  $\Delta t$  with respect to the transverse-current pulse,

$$\mathcal{E}_T(t) = E_T e^{i\omega t} \hat{e}_{\vec{v} \times \vec{B}}.$$

The angular position of the antenna with respect to the  $\hat{e}_{\vec{v} \times \vec{B}}$ -direction is denoted by  $\phi$ . The Stokes parameters now read

$$\begin{aligned} I &= E_T^2 + E_C^2 + 2 E_T E_C \cos \phi \cos \omega \Delta t \\ Q &= E_T^2 + E_C^2 \cos(2\phi) + 2 E_T E_C \cos \phi \cos \omega \Delta t \\ U &= E_C^2 \sin(2\phi) + 2 E_T E_C \sin \phi \cos \omega \Delta t \\ V &= 2 E_T E_C \sin \phi \sin \omega \Delta t. \end{aligned} \quad (3.1)$$

Extreme values for the circular polarization are reached for  $\phi = \pi/2$  and  $\phi = -\pi/2$ . Thus  $V/U = \tan \omega \Delta t$  measures the time-lag, between charge excess and geomagnetic radiation.

As an illustrative example we focus on an air shower for which the radio signal was detected in six LOFAR stations. The Stokes parameters extracted for each LOFAR antenna is shown versus

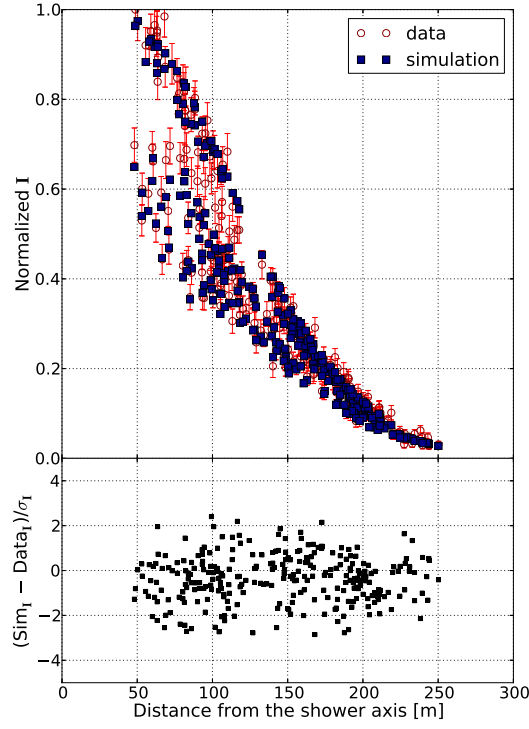


**Figure 1:** The measured intensity footprint of a shower (open red circles) is compared to the results of a CoREAS simulation (filled blue squares). The standard deviation is denoted by  $\sigma$ .

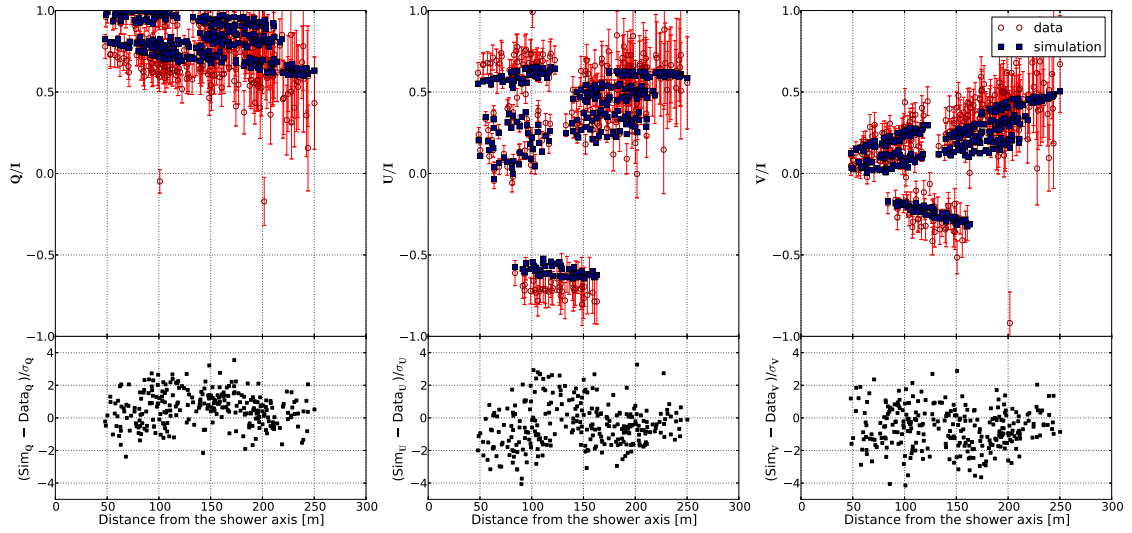


**Figure 2:** The normalized Stokes parameters for the air shower shown in Fig.1 where the meaning of the different symbols is also indicated.

distance to the shower axis in Fig. 1 and Fig. 2. The CoREAS simulation was done for  $X_{\max} = 659 \text{ g/cm}^2$ , shower energy  $E = 6.24 \times 10^{17} \text{ eV}$ , and zenith angle  $\theta = 26^\circ$ . The calculated values for  $W/I$  (not shown) are vanishingly small while the measured values for  $W/I$ , due to noise, increase from less than a percent at small distances to about 10% at larger distances. The scatter of the points at a fixed distance is due to the dependence of the Stokes parameters on the azimuthal position of the antenna, see Eq. (3.1).

Understanding the difference in the relative timing of the two radio pulse requires looking in detail into the two emission mechanisms. Taking the  $z$ -axis along the shower and the  $x$ -axis along  $\hat{e}_{\vec{v} \times \vec{B}}$  the vector potential due to transverse current is

$$A^\mu = j^\mu / D = j^x(t_{\text{ret}}) / D \quad (3.2)$$

where  $j^\mu$  is the four current induced in the plasma cloud of the EAS and  $D$  the retarded distance [12]. The retarded time is related to the emission height,  $t_{\text{ret}} = -z/c$ . The current induced by the Lorentz force is roughly proportional to the number of charged particles in the plasma cloud,  $N(t_{\text{ret}})$ , thus  $j^x(t_{\text{ret}}) \propto N(t_{\text{ret}})$  [23]. The charge excess in the plasma cloud, that moves with the speed of light to Earth, gives rise to a time and  $z$ -component of the current. Since the charge excess, like the geomagnetic current, is also roughly proportional to the lepton number in the cloud we obtain  $j^0(t_{\text{ret}}) \propto N(t_{\text{ret}})$ . Only due to a different dependence on air pressure and shower age a slight difference in the height (or retarded time) dependence of the two currents is induced and the transverse current reaches its maximum at somewhat larger heights than the charge excess [12].

To understand the circular polarization one has to go through the derivation of the radiation field from the vector potential

$$\vec{E} = -\vec{\nabla}A^0 - d\vec{A}/dt. \quad (3.3)$$

This yields  $\vec{E} = -d\vec{A}/dt$  for the transverse current contribution. Since this is like the emission from an varying electric current we call this magnetic emission. For the charge excess contribution we obtain  $\vec{E} = -dA^0/dr$ . Since this is similar to the radiation from a charge we call this electric and it is polarized in the radial,  $\hat{r}$  direction. For a fixed emission height the time and radial derivatives are related through [23]  $dt_{\text{ret}}/dt \approx c(R/r)dt_{\text{ret}}/dr$  where  $R$  is the distance to the emission point. Even if the charge excess and geomagnetic currents are assumed to have the same dependence on height in the atmosphere we now have obtained that the main contribution to the received intensity is lower in the atmosphere for charge excess than for geomagnetic. Numerical simulations show that this difference is about 1 km, depending on zenith angle of the cosmic ray.

This difference in emission height is schematically indicated in Fig. 3 left side where the curves labeled 'GeoMagnetic' and 'ChargeX' denote the height dependence of contribution of the different processes to the received signal. Due to the resulting difference in arrival time of the peak intensity for the two components the net polarization direction of the detected signal will rotate over an angle  $\phi$ . The angle  $\phi$  is the azimuthal position of the observer with respect to the  $\vec{v} \times \vec{B}$ -axis and is thus the same as the angle between the polarization directions of the geomagnetic and the charge-excess emissions, as indicated in the figure. It is thus clear that the circular polarization depends on the azimuthal position of the observer, as can be read from Eq. (3.1). This azimuthal dependence of the circular polarization can also be seen from the figure at the right side of Fig. 3 where the data and simulation for the footprint of the Stokes parameter  $V$  are compared. As expected,  $\hat{e}_{\vec{v} \times \vec{B}}$

is the axis of anti-symmetry, where the circular polarization has a different sign for points above or below this axis.

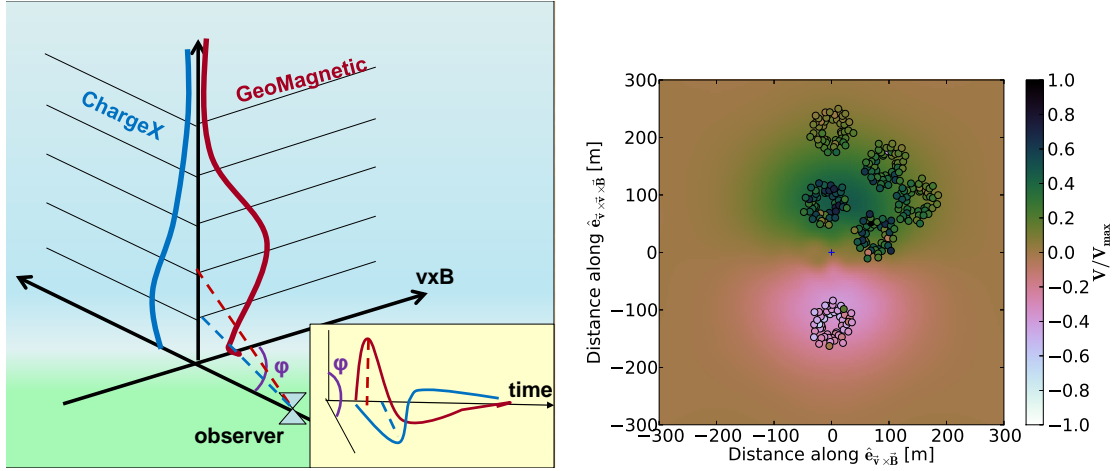


**Figure 3:** Schematic picture showing the source of circular polarization. Right side shows The footprint of the value of the Stokes V-parameter for a measured air shower. The background color shows the results of the CoREAS simulation while the coloring in the small circles presents the data. This is the same data as shown in Fig.2 (right most panel).

An equivalent explanation, based on the arguments given in the introduction is that the polarization is given by the projection of the inducing current on a direction perpendicular to the propagation direction of the radiation. The amplitude is proportional to the magnitude of the projected current. For geomagnetic emission the inducing current is in the  $\vec{v} \times \vec{B}$  direction which is already almost perpendicular to the line of sight. For charge excess radiation the inducing current is along the shower axis which implies that the projection perpendicular to the line of sight is small near the core of the shower and increases with distance. This also implies that emission from lower parts of the EAS are favored due to the projection factor. This leads to the same conclusion as we just arrived at, i.e. that even with the same height dependence of the inducing currents the charge excess radiation is effectively emitted at lower heights compared to geomagnetic radiation resulting in circular polarization of the signal.

#### 4. Conclusions & Summary

We have made a detailed investigation of the circular polarization of the radio emission of an EAS recorded under fair weather circumstances. We have given an interpretation based on macroscopic currents as are expected in an EAS and shown that it is due to a slight time delay between the charge excess and the geomagnetic pulse. This interpretation is supported by microscopic calculations using CoREAS that shows an almost perfect agreement with the data measured at LOFAR for all Stokes parameters.

Having shown that the full set of measured Stokes parameters for an event detected under fair weather conditions are quantitatively and quantitatively understood allows to use EAS as a diagnostics tool to extract atmospheric electric fields [17, 24].



## Acknowledgements

The LOFAR cosmic ray key science project acknowledges funding from an Advanced Grant of the European Research Council (FP/2007-2013) / ERC Grant Agreement n. 227610. The project has also received funding from the European Research Council (ERC) under the European Union's Horizon 2020 research and innovation programme (grant agreement No 640130). We furthermore acknowledge financial support from FOM, (FOM-project 12PR3041-3) and NWO (Top Grant 614-001-454, and Spinoza Prize SPI 78-409). AN is supported by the DFG (research fellowship NE 2031/1-1).

LOFAR, the Low Frequency Array designed and constructed by ASTRON, has facilities in several countries, that are owned by various parties (each with their own funding sources), and that are collectively operated by the International LOFAR Telescope foundation under a joint scientific policy.

## References

- [1] A. Nelles *et al.*, “The radio emission pattern of air showers as measured with LOFAR - a tool for the reconstruction of the energy and the shower maximum”, *J. Cosm. and Astrop. Phys.* **05**, 018 (2015); [arXiv:1411.7868](#).
- [2] A. Aab *et al.*, “Energy Estimation of Cosmic Rays with the Engineering Radio Array of the Pierre Auger Observatory”, *Phys.~Rev.~D* **93**, 122005 (2016); [arXiv:1508.04267](#).
- [3] S. Buitink *et al.*, “Method for high precision reconstruction of air shower  $X_{\max}$  using two-dimensional radio intensity profiles”, *Phys.~Rev.~D* **90**, 082003 (2014).
- [4] T. Huege, “Radio detection of cosmic ray air showers in the digital era”, *Phys. Rep.* **620**, 1 (2016); [arXiv:1601.07426](#).
- [5] W.D. Apel *et al.*, “Reconstruction of the energy and depth of maximum of cosmic-ray air-showers from LOPES radio measurements”, *Phys.~Rev.~D* **90**, 062001 (2014).
- [6] S. Buitink *et al.*, “A large light-mass component of cosmic rays at  $10^{17}$ – $10^{17.5}$  electronvolts from radio observations”, *Nature* **531**, 70 (2016).
- [7] T. Huege, M. Ludwig, and C. James, “Simulating radio emission from air showers with CoREAS”, *AIP Conf. Proc.* **1535**, 128 (2012).
- [8] J. Alvarez-Muñiz *et al.*, “Monte Carlo simulations of radio pulses in atmospheric showers using ZHAireS”, *Astropart. Phys.* **35**, 325 (2012).
- [9] P. Schellart *et al.*, “Detecting cosmic rays with the LOFAR radio telescope”, *Astron. & Astrophys.* **560**, A98 (2013); [arXiv:1311.1399](#).
- [10] A. Nelles *et al.*, “Measuring a Cherenkov ring in the radio emission from air showers at 110-230 MHz with LOFAR”, *Astropart. Phys.* **65**, 11 (2015); [arXiv:1411.6865](#).
- [11] D. Ardouin *et al.*, “Radiodetection of cosmic ray extensive air showers: Upgrade of the CODALEMA experiment”, *Int. J. Mod. Phys. A* **20**, 6869 (2005).
- [12] K.D. de Vries *et al.*, “The lateral distribution function of coherent radio emission from extensive air showers: Determining the chemical composition of cosmic rays”, *Astropart. Phys.* **34**, 267 (2010).

- [13] G.A. Askaryan, “*Excess negative charge of an electron-photon shower and its coherent radio emission*”, Sov. Phys. JETP **14**, 441 (1962).
- [14] V. Marin, for the CODALEMA Collaboration, “*Charge excess signature in the CODALEMA data; Interpretation with SELFAS2*”, Proc. 32<sup>nd</sup> ICRC, Beijing, **1**, 291 (2011).
- [15] H. Schoorlemmer, for the Pierre Auger Collaboration, “*Results from polarization studies of radio signals induced by cosmic rays at the Pierre Auger Observatory*”, Nucl. Instr. and Meth. A **662**, S134 (2012).
- [16] A. Aab *et al.*, “*Probing the radio emission from air showers with polarization measurements.*”, Phys.~Rev.~D~ **89**, 052002 (2014); arXiv:1402.3677.
- [17] P. Schellart *et al.*, “*Polarized radio emission from extensive air showers measured with LOFAR*”, J. Cosm. and Astrop. Phys. **1410**, 014 (2014); arXiv:1406.1355.
- [18] A. Bellétoile *et al.*, “*Evidence for the charge-excess contribution in air shower radio emission observed by the CODALEMA experiment*”, Astropart. Phys. **69**, 50 (2015)
- [19] H. Schoorlemmer, “*Tuning in on cosmic rays.*”, PhD thesis, Radboud Univeristy Nijmegen, ISBN: 978-90-9027039-5, 2008.
- [20] O. Scholten *et al.*, “*Measurement of the circular polarization in radio emission from extensive air showers confirms emission mechanisms*”, Phys.~Rev.~D~ **94**, 103010 (2016).
- [21] K. D. de Vries, O. Scholten, and K. Werner, “*The air shower maximum probed by Cherenkov effects from radio emission*”, Astropart. Phys. **45**, 23 (2013); arXiv:arXiv:1304.1321.
- [22] M. P. van Haarlem *et al.*, “*LOFAR: The LOw-Frequency ARray*”, Astron. & Astrophys. **556**, A2 (2013); arXiv:1305.3550.
- [23] O. Scholten, K. Werner, and F. Rusydi, “*A Macroscopic Description of Coherent Geo-Magnetic Radiation from Cosmic Ray Air Showers*”, Astropart. Phys. **29**, 94 (2008); K. Werner and O. Scholten, “*Macroscopic Treatment of Radio Emission from Cosmic Ray Air Showers based on Shower Simulations*”, Astropart. Phys. **29**, 393-411 (2008).
- [24] T.N.G. Trinh *et al.*, “*Thunderstorm electric fields probed by extensive air showers through their polarized radio emission*”, Phys.~Rev.~D~ **95**, 083004 (2017).

# Circular polarization of radio emission from extensive air showers probes atmospheric electric fields in thunderclouds.

---

**T.N.G. Trinh<sup>1</sup>, O. Scholten<sup>1,2\*</sup>, A. Bonardi<sup>3</sup>, S. Buitink<sup>4</sup>, A. Corstanje<sup>3</sup>, U. Ebert<sup>5,6</sup>,  
H. Falcke<sup>3,7,8</sup>, B. M. Hare<sup>1</sup>, J.R. Hörandel<sup>3,7</sup>, P. Mitra<sup>4</sup>, K. Mulrey<sup>4</sup>, A. Nelles<sup>3,9</sup>,  
J.P. Rachen<sup>3</sup>, L. Rossetto<sup>3</sup>, C. Rutjes<sup>5</sup>, P. Schellart<sup>3,10</sup>, S. ter Veen<sup>3,8</sup>,  
S. Thoudam<sup>3,11</sup>, T. Winchen<sup>4</sup>**

<sup>1</sup> KVI-CART, University Groningen, P.O. Box 72, 9700 AB Groningen, The Netherlands

<sup>2</sup> Interuniversity Institute for High-Energy, Vrije Universiteit Brussel, Pleinlaan 2, 1050 Brussels, Belgium

<sup>3</sup> Department of Astrophysics/IMAPP, Radboud University, P.O. Box 9010, 6500 GL Nijmegen, The Netherlands

<sup>4</sup> Astrophysical Institute, Vrije Universiteit Brussel, Pleinlaan 2, 1050 Brussels, Belgium

<sup>5</sup> Center for Mathematics and Computer Science (CWI), PO Box 94079, 1090 GB Amsterdam, The Netherlands

<sup>6</sup> Department of Applied Physics, Eindhoven University of Technology (TU/e), PO Box 513, 5600 MB Eindhoven, The Netherlands

<sup>7</sup> NIKHEF, Science Park Amsterdam, 1098 XG Amsterdam, The Netherlands

<sup>8</sup> Netherlands Institute of Radio Astronomy (ASTRON), Postbus 2, 7990 AA Dwingeloo, The Netherlands

<sup>9</sup> Department of Physics and Astronomy, University of California Irvine, Irvine, CA 92697-4575, USA

<sup>10</sup> Department of Astrophysical Sciences, Princeton University, Princeton, NJ 08544, USA

<sup>11</sup> Department of Physics and Electrical Engineering, Linnéuniversitetet, 35195 Växjö, Sweden  
E-mail: [t.n.g.trinh@rug.nl](mailto:t.n.g.trinh@rug.nl), [Scholten@KVI.nl](mailto:Scholten@KVI.nl)

During thunderstorm conditions, radio emission from extensive air showers are influenced by atmospheric electric fields. We show that air showers recorded under thunderstorm have a larger amount of circular polarization than air showers measured in fair weather. We demonstrate quantitatively that this is related to the change of the transverse current in the shower front, which is caused by the variation of the atmospheric electric fields. Therefore, the use of the circular polarization data puts strong additional constraints on the structure of the atmospheric electric fields than what could be achieved by using only the radio intensity.

*35th International Cosmic Ray Conference ICRC217-  
10-20 July, 2017  
Bexco, Busan, Korea*

---

\*Speaker.

## 1. Introduction

Cosmic rays impinging on the Earth's atmosphere generate showers of secondary particles. The motion of electrons and positrons in the shower induce radio emission. During thunderstorms, atmospheric electric fields are strong and thus can affect air showers and their radio radiation [1, 2]. The change of intensity of radio emission from air showers during thunderstorms can be used to determine the atmospheric electric fields [1]. There are also large differences in circular polarization between a showers recorded in fair-weather (a fair-weather event) and showers measured during thunderstorms (a thunderstorm event) [3]. In this paper, we present the method to determine atmospheric electric fields from a combined analysis of the intensity data and the polarization signature of the radio signals.

The data for this work are taken from the Low-Band Antennas (LBA) of the LOw-Frequency ARay (LOFAR) radio telescope [4]. The LBAs operate in the frequency range of 30 MHz – 80 MHz and they are grouped into circular stations. The core of LOFAR, consists of 6 such stations, located in a 320 m diameter region. A trigger is obtained from a particle detector array, LOfar Radboud air shower Array (LORA) [5]. The measurements are done under both fair-weather and thunderstorm conditions.

## 2. Circular polarization in fair-weather events and thunderstorm events

In fair weather, electrons and positrons in the shower front are deflected in opposite directions by the Lorentz force exerted by the geomagnetic field [6, 7]. They form a transverse current and emit radiation polarized in the direction of the Lorentz force,  $\mathbf{v} \times \mathbf{B}$ , where  $\mathbf{v}$  is the velocity of the shower and  $\mathbf{B}$  is the geomagnetic field. A secondary contribution is from charge excess which is caused by a build-up of negative charge in the shower front [8, 9]. This produces a radio pulse polarized radially with respect to the shower axis and dependent on the azimuthal position of an observer. The signal observed on the ground is the combination of the two contributions. There is a delay in time of the charge-excess pulses with respect to the transverse-current pulses. As a result, there is a small amount of circular polarization where the magnitude and handedness depend on the distance and the azimuthal position of the observer with respect to the shower axis [10].

During thunderstorms, the radio emission from air showers is affected by atmospheric electric fields in thunderclouds. The electric field can be decomposed into two components,  $\mathbf{E}_{\parallel}$  and  $\mathbf{E}_{\perp}$ . The  $\mathbf{E}_{\parallel}$  which is parallel to the shower axis has very little effect on the radio emission in the frequency range of LOFAR LBAs [2], so it is set to 0 in this work. The  $\mathbf{E}_{\perp}$  component which is perpendicular to the shower axis changes the net transverse force acting on particles. As a result, the direction and magnitude of the transverse current change, which gives rise to a change in both intensity and polarizations of the radiation. The signals from the different heights are emitted in sequence when the air shower front, propagating with the speed of light  $c$ , passes through. The emitted radio signals travel with a lower velocity than the shower front,  $c/n$ , where  $n$  is the index of refraction. As a result, near the shower axis, the pulses from a larger height arrives with a delay with respect to the pulses from the lower height. This causes a change in the polarization angle over the duration of the pulse, which is seen as circular polarization. The circular polarization of thunderstorm events does not depend on the distance and the azimuth position of the observer.

During the period between June 2011 and January 2015, we recorded 118 fair-weather events [11] and 20 thunderstorm events [1] with radio signals detected in at least 4 LBA stations. Fig. 1 shows the amount of circular polarization ( $|V|/I$ ) within a 30 m radius of the shower axis given for 884 antennas recording fair-weather data and 183 antennas taking thunderstorm data. It can be seen from the figure that the circular polarization for fair-weather events is small near the shower axis while large differences are observed for thunderstorm events.

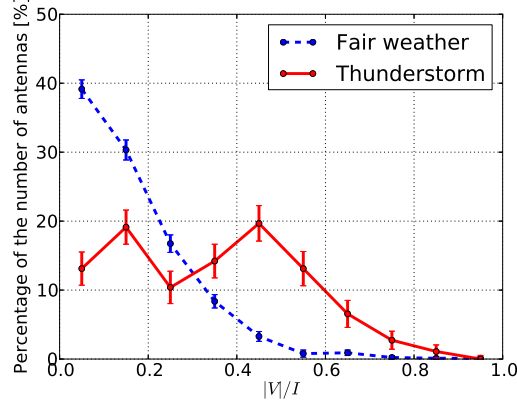


**Figure 1:** Distribution of the amount of circular polarization within a radius 30 m from the shower axis for showers measured during fair weather and thunderstorms.

### 3. Probing atmospheric electric fields

The circular polarization in thunderstorm events is caused by a variation in the orientation of the atmospheric electric fields. Therefore, using the combination of intensity, linear polarization, and circular polarization allows for a more accurate determination of the electric fields in the thunderclouds where the air shower passes through than when using only intensity information as in Ref. [1]. For this reason, we do the fitting for the full set of Stokes parameters [10].

Fitting thunderstorm events is challenging because the atmospheric electric fields contain many parameters. The number of parameters depends on the model of the electric field. In this work, we use a three-layer model which is also seen in charge-cloud structure and measured by balloon measurements. The electric fields are labeled with indices 1, 2 and 3 where 1 is the top layer. Each layer is defined by the height  $h$  above the ground where the electric field starts, the strength and the direction of the field  $\mathbf{E}_\perp$ . Hence, together with  $X_{max}$ , there are 10 parameters which make a grid search impossible. A possible method to find the minimum in the chi-square surface is the steepest descent procedure. In order to use this method, one needs to make sure that a small change in the radio footprints is due to a small change in the parameters of the electric field and not due to shower-to-shower fluctuations. In addition, since the calculation needs to be iterated many times, a single calculation should not take much computer time. For these reasons, we use EVA-l code [12] to get close to the optimal choice after which we use CoREAS [13] for the final calculations. In order to avoid obtaining a local minimum, for each thunderstorm event, we do 30 optimization runs with different initial values of parameters, using EVA-l. Fig. 2 shows the current

profiles of the calculations that have a small reduced  $\chi^2$  for a thunderstorm event. The values of the reduced  $\chi^2$  are represented by the thickness of the curves. The thicker the curve is, the smaller the reduced  $\chi^2$  is. At heights lower than 6 km, these current profiles are almost the same. There are some differences at high altitudes, but the radio-emission contribution at these heights is at large distances from the shower axis where the signal is weak. Therefore, it can be concluded that the results which we obtain are unique.

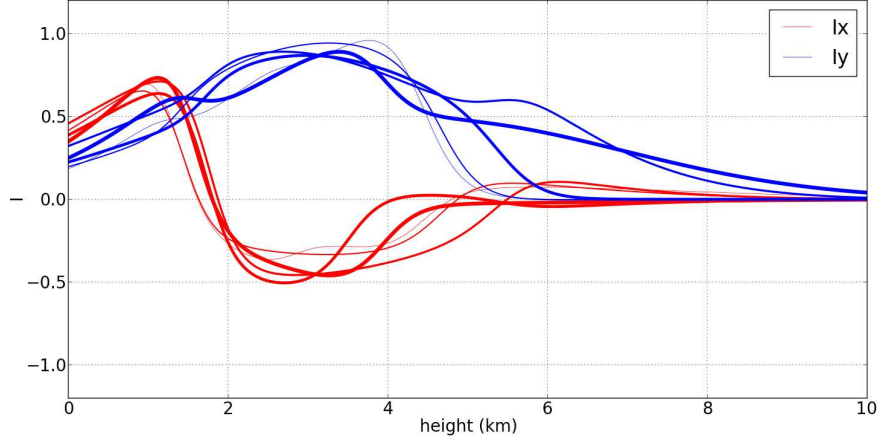


**Figure 2:** The current profiles of different calculations having small reduced  $\chi^2$ .

Fig. 3, Fig. 4 and Fig. 5 show the intensity footprint, the linear polarization footprint and the circular polarization footprint, respectively, of this event. The fractional Stokes parameters with their differences from the data are displayed in Fig. 6 to show the quality of the fit. The intensity footprint of this event (see Fig. 3) shows a bean shape which is also observed in fair-weather event but the maximum intensity is not in the  $\mathbf{v} \times \mathbf{B}$ -direction. The polarization footprint (see Fig. 4) shows a wavy pattern which is not shown in fair-weather events. We also observe a large fraction of circular polarization (see Fig. 5), which varies with distance from the shower axis. Since the polarization signature of this event is different from that of fair-weather events, using only the intensity data for this event gives incomplete information about the atmospheric electric field.

The values of the parameters giving the best fit are shown in Table. 1 together with  $X_{max} = 665 \text{ g/cm}^2$ . There are some differences between the measured and simulated Stokes parameters seen in Fig. 6 since the three-layered electric field is still an oversimplification of the realistic field. The reduced  $\chi^2$  for a joint fit of both the Stokes parameters and the particle data is  $\chi^2/\text{ndf} = 4.5$ , which is large compared to  $\chi^2/\text{ndf} \approx 1$  found in fair-weather showers. However, all main features are reproduced.

We have checked that the fit quality is sensitive to the heights of the layers on the order of hundred meters and the orientations of the electric fields at the level of degrees. However, the fit is not sensitive to heights above 8 km since there are few particles in the shower at this height and thus their contribution to the total radio emission is small. In the frequency range of LBAs, there is little sensitivity to the parallel component of electric fields. We are able to measure large horizontal components of the electric fields as explained in the following. A strict vertical electric field can

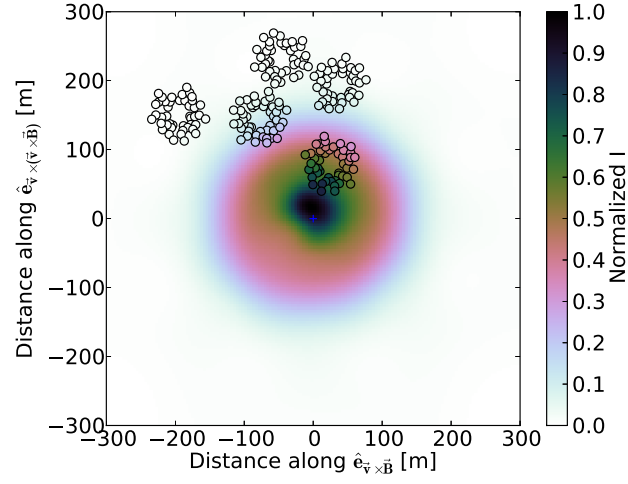


**Figure 3:** The intensity (Stokes I parameter) footprint of the thunderstorm event No.1. The background color shows the simulated results while the coloring in the small circles represents the data.

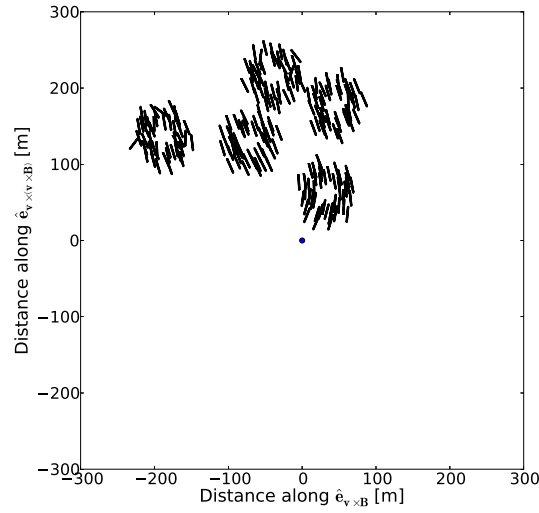


**Figure 4:** Linear polarization as measured with individual LOFAR LBAs (lines) in the shower plane.

Layer	1	2	3
Height (km)	8 - 5	5 - 2	2 - 0
$ \vec{E}_\perp $ (kV/m)	50	15	9
$\alpha$ ( $^\circ$ )	98	98	8
$E_{\mathbf{v} \times \mathbf{z}}$ (kV/m)	46	13	4
$E_{\mathbf{v} \times \mathbf{v} \times \mathbf{z}}$ (kV/m)	-22	-9	8

**Table 1:** The structure of the three-layered electric field of the thunderstorm event.



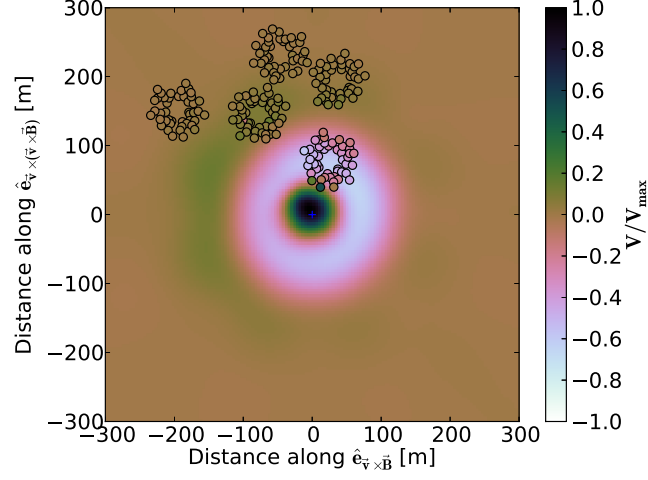


**Figure 5:** The footprint of Stokes V parameter, representing the circular polarization. The background color shows the simulated results while the coloring in the small circles represents the data.

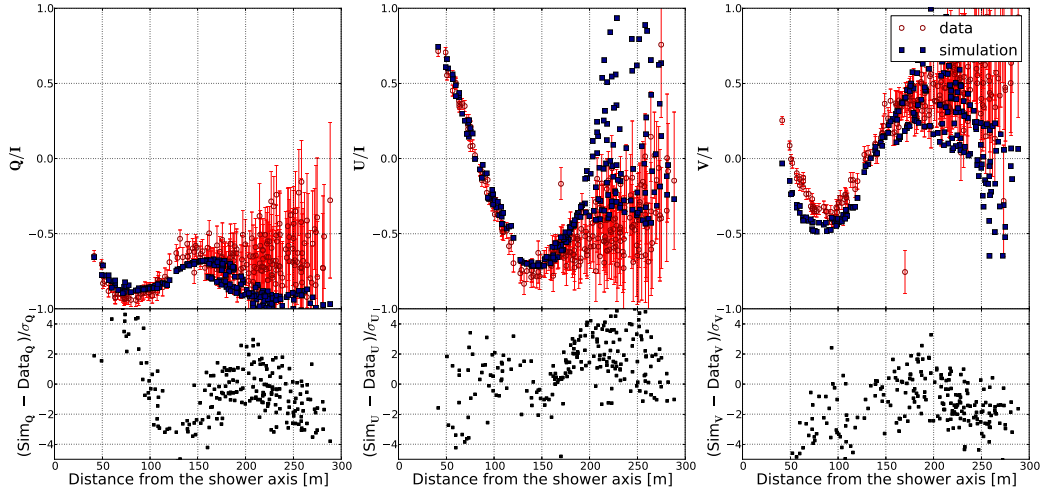


**Figure 6:** The set of normalized Stokes parameters of a thunderstorm event as recorded with the LOFAR LBAs (open red circles) is compared to the results of the CoREAS simulation (filled blue dots).  $\sigma$  denotes one standard deviation error.

be decomposed into two components, along  $\hat{e}_v$  and  $\hat{e}_v \times \hat{v} \times \hat{z}$ . Therefore, measuring a component in  $\hat{e}_v \times \hat{v} \times \hat{z}$  could thus be a reflection of a vertical field. However, a non-zero component in the  $\hat{e}_v \times \hat{z}$  direction (see Table. 1) can never be a projection of a purely vertical electric field, and is thus a genuine signature of a horizontal component.

#### 4. Conclusion

At LOFAR we have measured a large circular polarization component near the shower axis



in thunderstorm events while it vanishes near the core for fair-weather events. This is caused by the fact that the orientation of atmospheric electric fields changes with height, which gives rise to a rotation in the direction of the transverse current as the air shower proceeds towards the surface of the Earth. Therefore, using the full set of the Stokes parameters strongly improves the determination of the atmospheric electric fields in thunderclouds.

## 5. Acknowledgements

The LOFAR cosmic ray key science project acknowledges funding from an Advanced Grant of the European Research Council (FP/2007-2013) / ERC Grant Agreement n. 227610. The project has also received funding from the European Research Council (ERC) under the European Union's Horizon 2020 research and innovation programme (grant agreement No 640130). We furthermore acknowledge financial support from FOM, (FOM-project 12PR304) and NWO (VENI grant 639-041-130). AN is supported by the DFG (research fellowship NE 2031/1-1).

LOFAR, the Low Frequency Array designed and constructed by ASTRON, has facilities in several countries, that are owned by various parties (each with their own funding sources), and that are collectively operated by the International LOFAR Telescope foundation under a joint scientific policy.

## References

- [1] P. Schellart et al., *Probing atmospheric electric fields in thunderstorms through radio emission from cosmic-ray-induced air showers*, *Phys. Rev. Lett.* **114** (2015) 165001.
- [2] T. N. G. Trinh et al., *Influence of atmospheric electric fields on the radio emission from extensive air showers*, *Phys. Rev. D* **93** (2016) 023003.
- [3] T. N. G. Trinh et al., *Thunderstorm electric fields probed by extensive air showers through their polarized radio emission*, *Phys. Rev. D* **95** (2017) 083004.
- [4] M. P. van Haarlem et al., *Lofar: The low-frequency array*, *A&A* **556** (2013) A2.
- [5] S. Thoudam et al., *Lora: A scintillator array for {LOFAR} to measure extensive air showers*, *Nuclear Instruments and Methods in Physics Research Section A: Accelerators, Spectrometers, Detectors and Associated Equipment* **767** (2014) 339 – 346.
- [6] F. D. Kahn and I. Lerche, *Radiation from Cosmic Ray Air Showers*, *Royal Society of London Proceedings Series A* **289** (1966) 206–213.
- [7] O. Scholten, K. Werner, and F. Rusydi, *A macroscopic description of coherent geo-magnetic radiation from cosmic-ray air showers*, *Astroparticle Physics* **29** (2008), no. 2 94 – 103.
- [8] G. Askaryan, *Excess Negative Charge of the Electron-Photon Shower and Coherent Radiation Originating from It. Radio Recording of Showers under the Ground and on the Moon*, *J. Phys. Soc. Japan* **Vol: 17, Suppl. A-III** (1962).
- [9] K. D. de Vries et al., *Coherent cherenkov radiation from cosmic-ray-induced air showers*, *Phys. Rev. Lett.* **107** (2011) 061101.
- [10] O. Scholten et al., *Circular polarization in radio emission from extensive air showers*, . Accepted by *Phys. Rev. D* (11/2016).

- [11] S. Buitink et al., *A large light-mass component of cosmic rays at  $10^{17} - 10^{17.5}$  ev from radio observations*, *Nature* **531** (2016) 70–73.
- [12] O. Scholten et al., *Analytic calculation of radio emission from extensive air showers subjected to atmospheric electric fields*, *ARENA proceeding* (2016).
- [13] T. Huege, M. Ludwig, and C. W. James, *Simulating radio emission from air showers with coreas*, *AIP Conference Proceedings* **1535** (2013), no. 1 128–132.

# Study of the LOFAR radio self-trigger and single-station acquisition mode

---

**A. Bonardi<sup>\*1</sup>, S. Buitink<sup>2</sup>, A. Corstanje<sup>1</sup>, H. Falcke<sup>1,3,4</sup>, B.M. Hare<sup>5</sup>, J.R. Hörandel<sup>1,3</sup>, P. Mitra<sup>2</sup>, K. Mulrey<sup>2</sup>, A. Nelles<sup>1,6</sup>, J.P. Rachen<sup>1</sup>, L. Rossetto<sup>1</sup>, P. Schellart<sup>1,8</sup>, O. Scholten<sup>5,7</sup>, S. ter Veen<sup>1,4</sup>, S. Thoudam<sup>1,9</sup>, T.N.G. Trinh<sup>5</sup>, T. Winchen<sup>2</sup>**

<sup>1</sup> *Department of Astrophysics/IMAPP, Radboud University, P.O. Box 9010, 6500 GL Nijmegen, The Netherlands*

<sup>2</sup> *Astrophysical Institute, Vrije Universiteit Brussel, Pleinlaan 2, 1050 Brussels, Belgium*

<sup>3</sup> *NIKHEF, Science Park Amsterdam, 1098 XG Amsterdam, The Netherlands*

<sup>4</sup> *Netherlands Institute of Radio Astronomy (ASTRON), Postbus 2, 7990 AA Dwingeloo, The Netherlands*

<sup>5</sup> *KVI-CART, University Groningen, P.O. Box 72, 9700 AB Groningen, The Netherlands*

<sup>6</sup> *Department of Physics and Astronomy, University of California Irvine, Irvine, CA 92697-4575, USA*

<sup>7</sup> *Interuniversity Institute for High-Energy, Vrije Universiteit Brussel, Pleinlaan 2, 1050 Brussels, Belgium*

<sup>8</sup> *Department of Astrophysical Sciences, Princeton University, Princeton, NJ 08544, USA*

<sup>9</sup> *Department of Physics and Electrical Engineering, Linnéuniversitetet, 35195 Växjö, Sweden*

*E-mail: [a.bonardi@astro.ru.nl](mailto:a.bonardi@astro.ru.nl)*

The LOw Frequency ARay (LOFAR) observatory is a multipurpose radio antenna array aimed to detect radio signals in the frequency range 10 – 240 MHz. Radio antennas are clustered into over 50 stations, and are spread along Central and Northern Europe. The LOFAR core, where the density of stations is highest, is instrumented with the LOfar Radboud air shower Array (LORA), covering an area of about 300 m diameter centered at the LOFAR core position. Since 2011 the LOFAR core has been used for detecting radio-signals associated to cosmic-ray air showers in the energy range  $10^{16} - 10^{18}$  eV. Data acquisition is triggered by the LORA scintillator array, which provides energy, arrival direction, and core position estimates of the detected air shower too. Thus only the core of the LOFAR array is currently used for cosmic-ray detection.

In order to extend the energy range of the detected cosmic rays, it is necessary to expand the effective collecting area to the whole LOFAR array. On this purpose, a detailed study about the LOFAR potentialities of working in self-trigger mode, i.e. with the cosmic-ray data acquisition trigger provided by the radio-antenna only, is presented here.

A new method based on the intensity and the frequency spectrum for determining the air shower position to be implemented on LOFAR remote stations is presented too.

*35th International Cosmic Ray Conference — ICRC2017  
12–20 July, 2017  
Bexco, Busan, Korea*

---

<sup>\*</sup>Speaker.

## 1. Introduction

When a cosmic ray interacts with a nucleus of the Earth’s atmosphere, an Extensive Air Shower (hereafter “EAS”) of secondary particles is started. Associated with the EAS, a radio signal is emitted through Geo-magnetic radiation and Askaryan process. It has been recently proven that the primary particle properties, such as arrival direction, energy, and mass composition, can be reconstructed by ground-based radio detector arrays [1, 2, 3] with an accuracy similar to current cosmic-ray experiments. Compared to current EAS detectors, which are mainly based on Fluorescence detection or a combined system of particle detectors and fluorescence detectors [5], [6], [7], the main advantage of the Radio-detection technique is its duty cycle up to 100% and its considerably lower construction and operational costs. On the other hand, given the duration of the radio signal (less than 100 ns) and the overwhelming background noise of Radio-Frequency Interferences (hereafter “RFI”) for most of the available locations, the direct detection of EAS with radio detectors only has been very difficult so far. An additional issue is set by the need of a very accurate EAS core position reconstruction during the analysis of the radio data. Therefore, particle detectors have often been used in combination with radio antennas.

The LOw-Frequency ARray (LOFAR) [8] is a multipurpose radio antenna array aimed to detect radio signals in the frequency range 10 – 240 MHz. Radio antennas are clustered into over 50 stations, and are spread along Central and Northern Europe, with a higher density in the Northern Netherlands. Each LOFAR station is equipped with 96 omnidirectional Low-frequency Band Antennas (hereafter “LBA”), operational in the 10 – 90 MHz frequency band, and 96 High-frequency Band Antennas (hereafter “HBA”), operational in the 120 – 240 MHz frequency band. Both HBA and LBA have two polarization arms (hereafter “dipoles”) NE-SW and NO-SE oriented but, due to the different antenna geometry, only LBA can observe the full-sky at once. Therefore, HBA are rarely used for cosmic-ray detection and are not discussed any further in this work. During standard astronomical observations, on each station only half of LBA are active in the so-called “LBA inner” or “LBA outer” configuration, as shown in Fig. 1-left, with a large predominance of LBA outer observations.

The LORA (LOfar Radboud air shower Array) [4] particle detector array covers the region of the LOFAR core, i.e. the region with the highest density of stations, corresponding to a circular area of about 300 m diameter as shown in Fig. 1-right. The main task of LORA is to provide the trigger to the LOFAR array: when an EAS is detected, the time series data ( $\sim 2.2$  ms length, 200 MSample  $s^{-1}$ ) of each active antenna polarization arm is downloaded for the offline cosmic-ray analysis. Moreover, the arrival direction, energy, and core position provided by LORA are used as starting values during the following radio data analysis. Since 2011 LOFAR antennas together with LORA have been successfully used for detecting radio-signals associated to EAS in the energy range  $10^{16} - 10^{18}$  eV falling within the LOFAR core region [1, 2, 3]. Given the current configuration, only a small fraction of the LOFAR array can be used for cosmic-ray detection. This sets a strong limit to the LOFAR capabilities of detecting cosmic rays at energies above  $10^{18}$  eV, where a large coverage area is essential. Unfortunately, expanding the LORA array to cover the full LOFAR array is unfeasible, because of the costs. Moreover, due to the scattered distribution of the LOFAR stations, the radio signal at ground level (hereafter “footprint”) of a cosmic ray falling out-

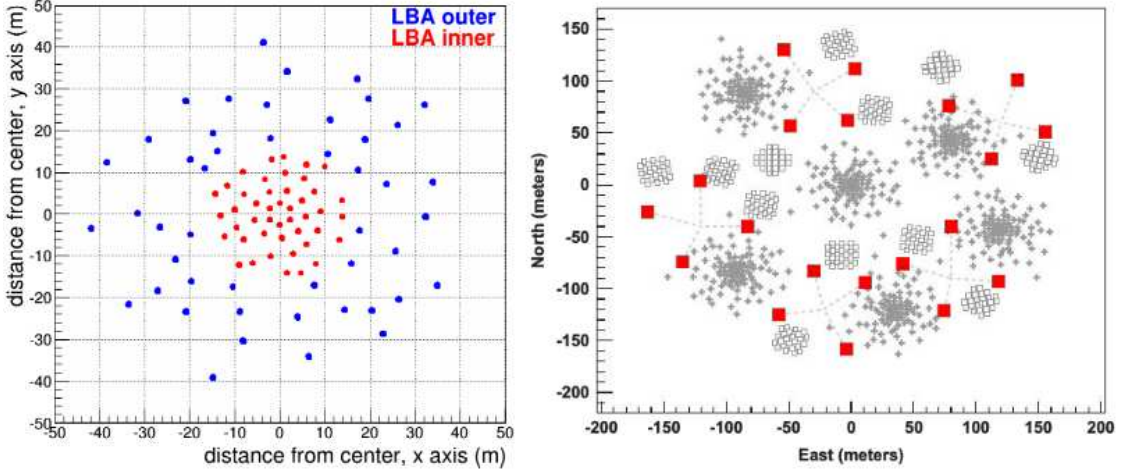


**Figure 1:** *Left:* Antenna location in one LOFAR station for LBA inner and LBA outer configuration. *Right:* LBA (black crosses), HBA (empty squares), and LORA detectors (red squares) position in the LOFAR core region.

side the LOFAR core is quite likely detectable by one station only. Therefore, in order to extend the cosmic-ray detection to the LOFAR remote stations, the following steps have to be implemented:

- **a radio self-trigger system:** a new trigger system based on the online analysis of the radio data, also known as “radio self-triggering”. The solution developed for LOFAR single stations is described in Section 2;
- **a single-station EAS core determination technique:** the LOFAR cosmic-ray analysis is very sensitive to the position of the EAS core. In case of single-station detection and no particle detector available, the current LOFAR method is not expected to have the required precision. The proposed new EAS core determination technique, based on radio pulse intensity and frequency spectrum, is described in Section 3.

## 2. The Radio self-trigger system

### 2.1 The algorithm

In order to overcome the first addressed issue, an algorithm for triggering individual LOFAR stations has been developed for the online recognition of cosmic rays. The developed algorithm consists of two separate steps: in the first step radio pulses are found (“selection phase”), while in the second one RFI-candidates, i.e. radio pulses which are believed to originate from RFI, are rejected (“RFI rejection phase”). During the selection phase, the radio signal of each dipole is compared with its baseline fluctuation: when a dipole shows a signal above the threshold, that dipole is considered as “fired”. A radio pulse is considered as “detected” if at least 24 antenna dipoles are fired along the same polarization within a coincidence time of 20 ns in the LBA inner configuration or 30 ns in the LBA outer configuration. The RFI rejection phase is based on a multi-criteria approach, consisting of evaluating the radio pulse duration, its frequency spectrum,

its timing, and its arrival zenith angle. Radio pulses satisfying any of the following conditions are treated as RFI and rejected:

- **pulse duration:** the time window where 3 or more antennas have a signal above threshold within the coincidence time is larger than 75 ns (LBA inner) or 300 ns (LBA outer);
- **frequency spectrum:** the ratio between the station mean pulse intensity in the 30 – 45 MHz frequency band and in the 45 – 70 MHz band is smaller than 1 or larger than 2;
- **timing:** the pulse occurs within 5  $\mu$ s before/after another detected pulse;
- **arrival direction:** its reconstructed direction of arrival is more than 60° from the zenith.

If a detected radio pulse passes the RFI rejection phase, the station is considered “triggered”.

## 2.2 Analysis and Results

We considered the raw-data from the 4081 events recorded with LBA outer configuration and the 634 events with LBA inner configuration, corresponding to about 9 s and 2 s LOFAR acquisition live-time, respectively. All those events have time, energy, position, and arrival direction successfully reconstructed by LORA, and have at least data for all antennas of one LOFAR station. Stations with one or more missing read-out channels have been discarded.

Four threshold levels, equal to 3, 4, 5, and 10 times the baseline RMS, have been considered for the dipole “firing” condition. The detected radio pulses are considered cosmic-ray signals if occurring within 5  $\mu$ s before and 12.5  $\mu$ s after the LORA time stamp. Any pulse falling outside this time window is considered as RFI pulse. The results obtained for LBA inner and LBA outer configurations are summarized in Table 1 and Table 2.

Threshold Level	CR detections	rejected CR detections	RFI triggers after rejection
3 RMS	395	65%	0
4 RMS	246	36%	0
5 RMS	168	27%	0
10 RMS	51	35%	0

**Table 1:** Trigger performances for LBA inner configuration

Threshold Level	CR detections	rejected CR detections	RFI triggers after rejection
3 RMS	1536	25%	4
4 RMS	899	21%	2
5 RMS	598	22%	2
10 RMS	196	24%	0

**Table 2:** Trigger performances for LBA outer configuration

For both LBA inner and LBA outer, the primary particle energy distributions of all the analyzed events and of the events generating a trigger in at least one station is shown in Fig. 2. The distributions of the trigger efficiency as function of the distance on the shower plane from the EAS core position is reported in Fig. 3 for the four considered threshold levels together with the detection efficiency of the LOFAR offline analysis.

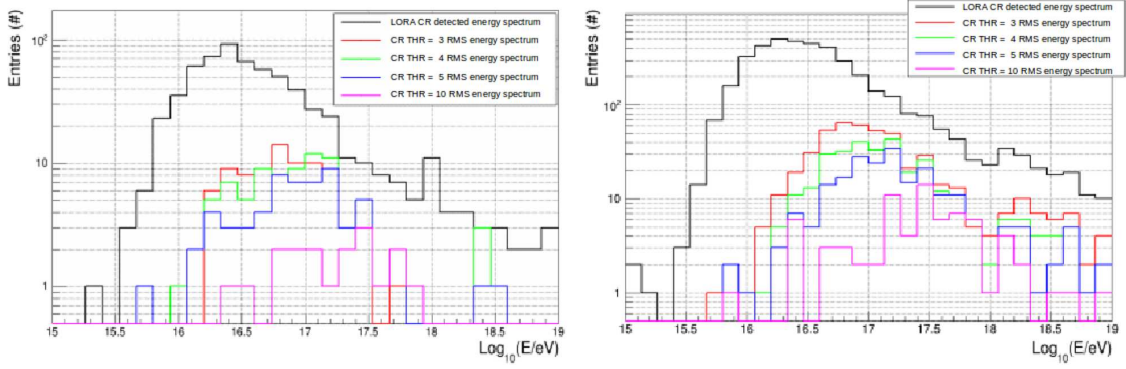


**Figure 2:** Primary particle energy distributions for LBA inner configuration (left) and LBA outer configuration (right), as reconstructed by LORA. The distribution of the whole set of events is shown together with the distribution of triggered events at trigger threshold equal to 3, 4, 5, and 10 RMS.

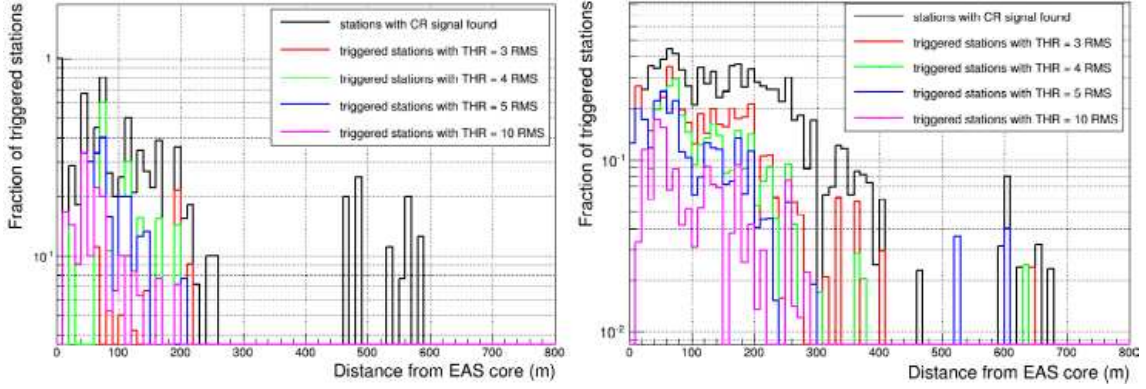


**Figure 3:** Station trigger efficiency as function of the distance from the LORA reconstructed EAS core position on the shower plane for LBA inner configuration (left) and LBA outer configuration (right) for events of energy above  $2 \cdot 10^{17}$  eV. For both distributions the detection efficiency with the LOFAR radio-data offline analysis is reported too.

### 3. The EAS core determination

The current LOFAR method for determining the core position of an EAS triggered by LORA and detected by LOFAR is based on an iterative analysis of the intensity Lateral Distribution Function (hereafter “LDF”) of the radio footprint, as discussed in [9] and [2]. The method has been optimized for cosmic rays falling within the LOFAR core region, that means with over 300 available antennas covering an area of approximately 300 m diameter. That method is not expected to work with the required accuracy for EAS detected by remote stations, where only 48 antennas concentrated on an area of approximately 80 m diameter are available.

From analytical calculations [10] the frequency spectrum of the radio footprint is expected to be function of the distance from the EAS core. Encouraging results have been obtained on that aspect by the Pierre Auger Observatory [11] and by LOFAR [12]. The new proposed method combines the analysis of the radio-pulse intensity, similarly to what is currently done, with the study of the radio-pulse frequency spectrum. The method is subdivided in the following steps:



- 1) **pulse timing:** on each active antennas, the peak of the sampled signal gives the time of the radio pulse  $t_0$ . Knowing the geometrical position of the antennas and by fitting the distribution of the found  $t_0$  values with a plane wavefront, the cosmic ray arrival direction is determined;
- 2) **pulse frequency spectrum:** the Fast Fourier Transform distribution (hereafter “FFT”) is computed for each antenna in a time window of 128 recorded samples, defined as  $[t_0 - 240 \text{ ns}, t_0 + 400 \text{ ns}]$ . A linear fit is performed on the logarithm of the FFT squared module distribution, i.e.  $\log_{10} |\text{FFT}|^2$ , in the 33-70 MHz frequency range. The frequency range has been selected to minimize both the RFI-contamination and the border effects of the antenna pass-band filter. The value of the slope  $s$  of the linear fit is then extracted;
- 3) **pulse intensity:** for each antenna, the intensity of the detected radio pulse is given by the S/N parameter, given by the formula

$$S/N = \frac{\int_{33 \text{ MHz}}^{70 \text{ MHz}} |FFT_S|^2 - |FFT_N|^2 d\nu}{\int_{33 \text{ MHz}}^{70 \text{ MHz}} |FFT_N|^2 d\nu}$$

where  $|FFT_S|^2$  is the squared module of the FFT of the radio pulse, as described at previous point, and  $|FFT_N|^2$  is the average of the squared module of the FFT computed in 400 time windows of 640 ns equally distributed before and after the radio pulse occurrence. Antennas showing  $S/N < 1$  are discarded from the analysis;

- 4) **parabolic fit:** the dependence of the parameter  $\zeta(d)$ , defined as

$$\zeta(d) = \frac{\log_{10}(S/N)}{\log_{10}(-s)}$$

versus the distance from the EAS core on the shower plane  $d$  is well represented by a parabolic function. By setting the position of the shower core  $(X_0, Y_0)$  *a priori*, a parabolic fit of the distribution of the parameter  $\zeta(d)$  is performed, and the corresponding  $\chi^2$  value computed. By repeating the fitting procedure for different  $(X_0, Y_0)$  positions, the final EAS core position in the shower plane is given by the  $(X_0, Y_0)$  value minimizing the  $\chi^2$  value.

In Fig. 4-left the distribution of the  $\zeta$  parameter versus the distance from the shower core is shown together its best parabolic fit for one well reconstructed EAS ( $E = 2.9 \cdot 10^{17} \text{ eV}$ ) falling within the LOFAR core region. In Fig. 4-right the  $\chi^2$  value distribution on the shower plane is reported for the same event, with the obtained EAS core position  $(X_0, Y_0)$  marked with a black star.

#### 4. Conclusions and Outlook

A detailed study about the potential to record extensive air showers with LOFAR in self-trigger mode has been carried out. For both LBA inner and LBA outer for cosmic-ray energy above  $2 \cdot 10^{17} \text{ eV}$ , a good trigger efficiency together with a very good RFI-rejection efficiency has been obtained. By considering data acquired during fair-weather conditions only, one RFI pulse

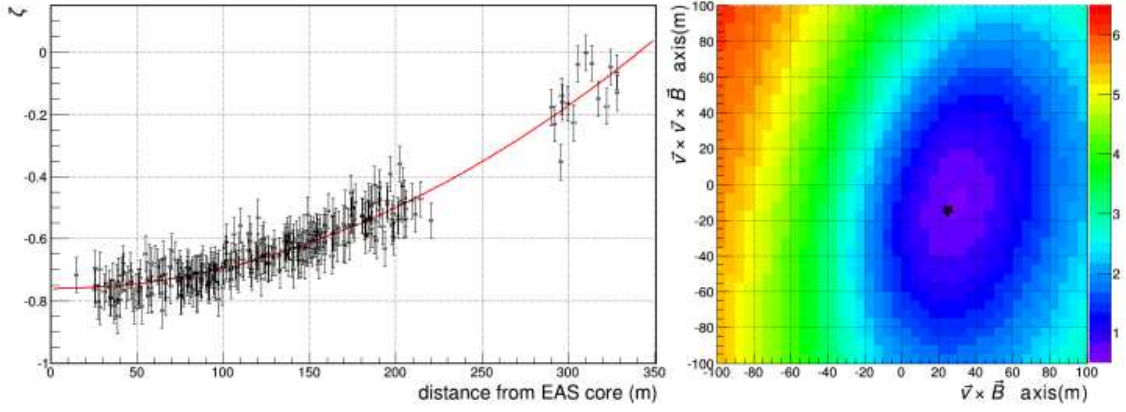


**Figure 4:** *Left:* distribution of the  $\zeta$  parameter versus the distance from the shower core together its best parabolic fit (in red) for a well reconstructed EAS falling within the LOFAR core region. *Right:*  $\chi^2$  distribution of the parabolic fit as function of the EAS core position on the shower plane along the  $\vec{v} \times \vec{B}$  and the  $\vec{v} \times \vec{v} \times \vec{B}$  directions, where  $\vec{v}$  is the cosmic ray moving direction and  $\vec{B}$  the Earth's magnetic field. The black star indicates the reconstructed core position. In the shown coordinates system, position (0, 0) is the core position as reconstructed by the current LDF analysis.

passed the rejection criteria only (THR = 3 RMS, LBA outer configuration). However, the available statistics is too low ( $\sim 9$  s LOFAR live-time or  $\sim 119$  s summing up all available stations for LBA outer, and  $\sim 2$  s LOFAR live-time or  $\sim 22$  s summing up all available stations for LBA inner) for concluding that the desired RFI rejection efficiency has been achieved. Low threshold data acquisitions are planned to be performed on one LOFAR test station for increasing the available statistics.

The results obtained about a new air shower reconstruction method are encouraging, even if still preliminary. It has been shown the  $\zeta$  parameter can be used for the EAS core position determination. The following step will be to determine the accuracy of the new method compared to the current ones and, afterwards, to apply the new method to single-station cases.

Once the RFI trigger rate is found to be smaller than 1 per hour per station and the new method for the EAS core determination is fine-tuned, the self-trigger algorithm will be implemented to the LOFAR remote stations, in order to extend the LOFAR cosmic-ray collecting area.

## Acknowledgments

The LOFAR cosmic ray key science project acknowledges funding from an Advanced Grant of the European Research Council (FP/2007-2013) / ERC Grant Agreement n. 227610. The project has also received funding from the European Research Council (ERC) under the European Union's Horizon 2020 research and innovation program (grant agreement No 640130). We furthermore acknowledge financial support from FOM, (FOM-project 12PR3041-3) and NWO (Top Grant 614-001-454, and Spinoza Prize SPI 78-409). AN is supported by the DFG (research fellowship NE 2031/1-1).

LOFAR, the Low Frequency Array designed and constructed by ASTRON, has facilities in several countries, that are owned by various parties (each with their own funding sources), and that are

collectively operated by the International LOFAR Telescope foundation under a joint scientific policy.

## References

- [1] A. Corstanje et al., *The shape of the radio wavefront of extensive air showers as measured with LOFAR*, *Astroparticle Physics* **61** (2015) 22 [astro-ph.HE/1404.3907]
- [2] A. Nelles et al., *The radio emission pattern of air showers as measured with LOFAR - a tool for the reconstruction of energy and shower maximum*, *Journal of Cosmology and Astroparticle Physics* **05** (2015) 18 [astro-ph.HE/1411.7868]
- [3] S. Buitink et al., *A large light-mass component of cosmic rays at  $10^{17} - 10^{17.5}$  electronvolts from radio observations*, *Nature* **531** (2016) 70 [astro-ph.HE/1603.01594]
- [4] S. Thoudam et al., *LORA: A scintillator array for LOFAR to measure extensive air shower*, *Nuclear Instruments and Methods in Physics Research Section A* **767** (2014) 339 [physics.ins-det/1408.4469]
- [5] J. Abraham et al., *The fluorescence detector of the Pierre Auger Observatory*, *Nuclear Instruments and Methods in Physics Research Section A* **620** (2010) 227 [astro-ph.IM/0907.4282]
- [6] I. Allekotte et al., *The surface detector system of the Pierre Auger Observatory*, *Nuclear Instruments and Methods in Physics Research Section A* **586** (2008) 409 [astro-ph/0712.2832]
- [7] H. Kawai et al., *Telescope Array Experiment*, *Nuclear Physics B (Proceedings Supplements)*, **175-176** (2008) 221
- [8] M. P. Van Haarlem et al., *LOFAR: The Low-Frequency ARray*, *Astronomy & Astrophysics* **556**, A2, 53, 2013 [astro-ph.IM/1305.3550]
- [9] A. Nelles et al., *A parameterization for the radio emission of air showers as predicted by CoREAS simulations and applied to LOFAR measurements*, *Astroparticle Physics* **60** (2015) 13 [astro-ph.HE/1402.2872]
- [10] T. Huege and H. Falcke, *Radio-Emission from Cosmic Ray Air Showers: Coherent Geosynchrotron Radiation*, *Astronomy & Astrophysics* **412** (2003) 019 [astro-ph/0309622]
- [11] S. Jansen, *PhD thesis, Radio for the Masses - Cosmic ray mass composition measurements in the radio frequency domain* (2016) ISBN 978 94 028 0073 9
- [12] L. Rossetto et al., *Characterisation of the radio frequency spectrum emitted by high energy air showers with LOFAR*, in proceedings of 35<sup>th</sup> ICRC, PoS (ICRC2017) 329 (2017)

# Expansion of the LOFAR Radboud Air Shower Array

---

**K. Mulrey<sup>1\*</sup>, A. Bonardi<sup>2</sup>, S. Buitink<sup>1</sup>, A. Corstanje<sup>2</sup>, H. Falcke<sup>2,3,4</sup>, B. M. Hare<sup>5</sup>,  
J. R. Hörandel<sup>2,3</sup>, P. Mitra<sup>1</sup>, A. Nelles<sup>2,6</sup>, J. P. Rachen<sup>2</sup>, L. Rossetto<sup>2</sup>, P. Schellart<sup>2,7</sup>,  
O. Scholten<sup>5,8</sup>, S. ter Veen<sup>2,4</sup>, S. Thoudam<sup>2,9</sup>, T. N. G. Trinh<sup>5</sup>, T. Winchen<sup>1</sup>**

<sup>1</sup> *Astrophysical Institute, Vrije Universiteit Brussel, Pleinlaan 2, 1050 Brussels, Belgium,*

<sup>2</sup> *Department of Astrophysics/IMAPP, Radboud University, P.O. Box 9010, 6500 GL Nijmegen, The Netherlands,*

<sup>3</sup> *NIKHEF, Science Park Amsterdam, 1098 XG Amsterdam, The Netherlands,*

<sup>4</sup> *Netherlands Institute of Radio Astronomy (ASTRON), Postbus 2, 7990 AA Dwingeloo, The Netherlands,*

<sup>5</sup> *KVI-CART, University Groningen, P.O. Box 72, 9700 AB Groningen,*

<sup>6</sup> *Department of Physics and Astronomy, University of California Irvine, Irvine, CA 92697-4575, USA,*

<sup>7</sup> *Department of Astrophysical Sciences, Princeton University, Princeton, NJ 08544, USA,*

<sup>8</sup> *Interuniversity Institute for High-Energy, Vrije Universiteit Brussel, Pleinlaan 2, 1050 Brussels, Belgium,*

<sup>9</sup> *Department of Physics and Electrical Engineering, Linnéuniversitetet, 35195 Växjö, Sweden*  
*E-mail: [kmulrey@vub.ac.be](mailto:kmulrey@vub.ac.be)*

The LOFAR Radboud Air Shower Array (LORA) consists of 20 plastic scintillators and is situated at the core of the LOFAR radio telescope. LORA detects particles from extensive air showers and triggers the read-out of the LOFAR antennas. The dense LOFAR antenna spacing allows for detailed sampling of the radio emission generated in extensive air showers, which yields high precision reconstruction of cosmic ray properties and information about the shower development. We discuss the proposed expansion of LORA, including the addition of scintillator units and the implementation of triggering algorithms that will probe more details of the radio emission and detect lower energy showers without introducing a composition bias, which is important for studying the origin of cosmic rays.

*35th International Cosmic Ray Conference -ICRC217-  
10-20 July, 2017  
Bexco, Busan, Korea*

---

\*Speaker.

## 1. Introduction

As air showers develop in the atmosphere, radio emission is generated through the charge excess effect and the transverse current induced by the magnetic field of the Earth. The resulting pattern of radiation on the ground is highly structured and information about the primary cosmic ray can be extracted from radio data [1]. Radio techniques have been used to reconstruct the energy, geometry, and composition of cosmic rays with high precision [2]. The LOw Frequency ARray (LOFAR) is particularly well suited to study radio emission from cosmic rays because of its dense antenna spacing [3, 4]. LOFAR is optimal for detecting air showers with energies between  $10^{16}$  and  $10^{18}$  eV where the transition from galactic to extra-galactic cosmic rays is expected to exist.

The LOfar Radboud Air shower array (LORA) is deployed in the LOFAR core as a means to trigger the LOFAR array and provide information about the primary cosmic ray based on particle data [5]. LORA data has been used to construct the cosmic ray energy spectrum between  $10^{16}$  and  $10^{18}$  eV [6]. Because of the steeply falling cosmic ray spectrum, most triggered events are low in energy, around  $10^{16}$  eV, where the radio signal is unlikely to be detectable above background noise. Additionally, a composition bias is introduced in the triggering scheme. We propose to add additional scintillators to the array in the LOFAR core, with the goal of increasing the usability of triggered events.

## 2. LORA

LORA currently consists of 20 plastic scintillators,  $0.95 \text{ m} \times 0.95 \text{ m}$  in size, arranged in 5 stations of 4 detectors. The scintillators were previously used in the KASCADE experiment [7]. Each LORA station is associated with a LOFAR low-band antenna (LBA) station and has an inter-scintillator spacing between 50 m and 100 m. The entire array spans 300 m across the LOFAR superterp, as shown in the left panel of Figure 1. LORA provides a trigger for LOFAR antenna readout when a given number of detectors have a strong enough signal to noise ratio. The threshold level for detection roughly corresponds to the amount of energy deposited in a scintillator by one muon. When at least one LORA station detects a signal in at least 3 out of 4 scintillators, information from all the stations is sent to a master computer. A high-level trigger is then formed to read out data from the active LOFAR antennas. Currently, LOFAR is triggered when 13 out of 20 scintillators have a signal. The trigger condition influences the trigger rate and the energy threshold for detection. The current condition ensures that the data read out rate at LOFAR remains manageable while minimizing triggers from events with energy lower than  $10^{16}$  eV.

At present, 19% of triggered events have a detectable cosmic ray radio signal, as determined by the data reduction pipeline [3]. This point is demonstrated in the right panel of Figure 1. The detected flux of cosmic rays with usable radio signals is shown, where the event energies are reconstructed using a fit to a two dimensional radio LDF [2, 8]. Radio signals become detectable above  $10^{16.5}$  eV. It is useful to compare events with usable radio signal with all events triggered with LORA. To do this, simulated air showers are used. Details of the simulation process are discussed in Section 3. Simulated flux is scaled to the measured data at  $10^{17.5}$  eV because the time of detection, and therefore flux, is not known, as operating conditions vary and are not continuous. The comparison illustrates that events with energies above  $10^{17}$  eV generally have a strong enough

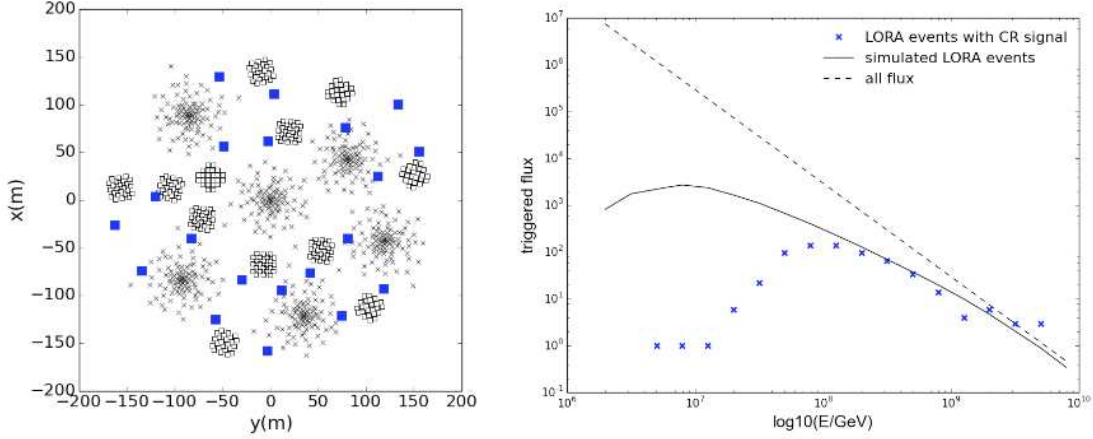


**Figure 1:** Left: Layout of the LORA array and LOFAR antennas in the superterp. Blue squares represent LORA detectors, black x's represent LBA antennas, and black boxes represent HBA antennas. Right: Measured and simulated cosmic ray fluxes. For measured LORA events, marked with blue crosses, all events with a detectable radio signal are included. For simulated events, the total flux of cosmic rays is multiplied by the probability of triggering LORA and scaled to the measured data at  $10^{17.5}$  eV, since the time frame of detection is unknown. 19% of triggered events are above  $10^{16.5}$  eV, and therefore have a likely detectable radio signal. The dashed line represents the total cosmic ray flux.

radio signal to be detected, and that the majority of triggered events do not have a detectable radio signal.

In order to trigger on only the high energy showers, the number of detectors necessary to form a LOFAR trigger could be increased. However, this reduces the trigger rate to an unnecessarily low level. Additionally, there is a bias introduced by the number of detectors required for a trigger. Since light primaries generally interact later in the atmosphere than heavy primaries, more shower particles reach the ground detection level. Therefore, light primary cosmic rays are more likely to trigger LORA than heavy primaries, as shown in Figure 2. Here, the probability of an event within 250 m of the LOFAR core triggering is plotted as a function of the number of detectors required for a LOFAR trigger. Below  $10^{17}$  eV, the probability of triggering 13 detectors is different for proton and iron primaries, and so a bias is introduced. It would be optimal to have a clean sample for energies down to  $10^{16.5}$  eV, which is interesting for source transition studies. In practice, some detected events have cores outside of 250 m radius, and so composition bias has to be studied on an event by event basis.

### 3. Simulations and Design consideration

Simulations have been used to determine the optimal layout of the LORA expansion. Air showers are generated with CORSIKA [9], using QGSJET II-04 [10] for energies above 200 GeV and FLUKA [11] for lower energies. Showers for proton and iron primaries are simulated for energies between  $10^{15}$  and  $10^{19}$  eV and for zenith angles between  $0^\circ$  and  $45^\circ$ . The flux is weighted to a -3 spectral index. Thinning is used at a level of  $10^{-6}$  [12]. For each shower, all ground level particles are projected into the shower plane, and collected in radial bands of 5 m. A GEANT4 [13]



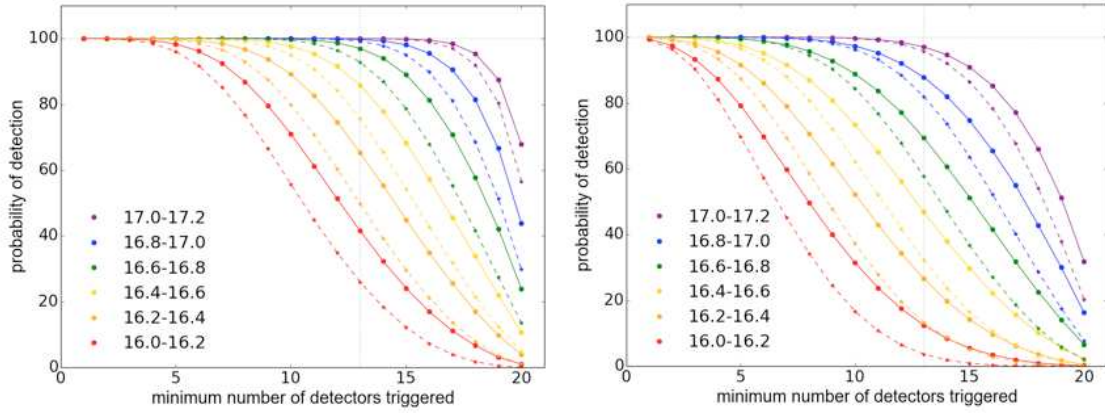


**Figure 2:** Probability of triggering a minimum number of detectors. Solid lines represent proton showers and dashed represent iron showers. Left: Zenith angles between  $0^\circ$  and  $30^\circ$ . Right: Zenith angles between  $30^\circ$  and  $45^\circ$ . The different colors represent different energy bands, as indicated in the legend as  $\log(\text{energy/eV})$ .

simulation with realistic LORA scintillator geometry is used to convert the particles at ground level into an energy deposit per  $\text{m}^2$  as a function of radius to the shower core in the shower plane. Each shower is then given 100 random positions within 2000 m of the center of the superterp. This distance is chosen to ensure that not all showers trigger LORA. The positions of the detectors are projected into the shower plane and assigned an energy deposit based on their position relative to the shower core.

For each shower, the number of detectors with signal is calculated. The current LORA signal threshold is the average energy deposited by one muon. Therefore, the simulated detectors are considered to contain a detectable signal if they contain the energy deposit of at least one muon, which from simulation is 6.4 MeV. The total energy in the detector is divided by this number, and then the final muon content of the detector is drawn from a Poisson distribution.

The placement of additional detectors on the ground is dictated by logistical considerations. Detectors can only be placed on land around current LOFAR stations, and must not interfere with current operations. Digitizing electronics are most convenient to use in sets of 2 or 4. For this reason, additional stations consist of 4 scintillators and are simulated in the locations of LOFAR LBA fields in rings of radius 50 m, as shown in Figure 3. In total 20 detectors are available for the expansion.

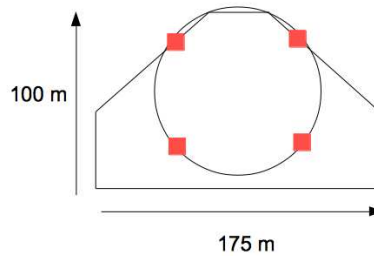


**Figure 3:** Simulated positions of detectors in additional stations.



New LORA layouts are achieved by adding new stations of four scintillators. This document includes 6 arrangements of note, as seen in Figure 4. The naming system indicates the total number of scintillators included. These arrangements were chosen to study the effects of detector spacing and the total number of scintillators used. For example, arrangement 40b has 5 new stations with farther spacing than 40a.

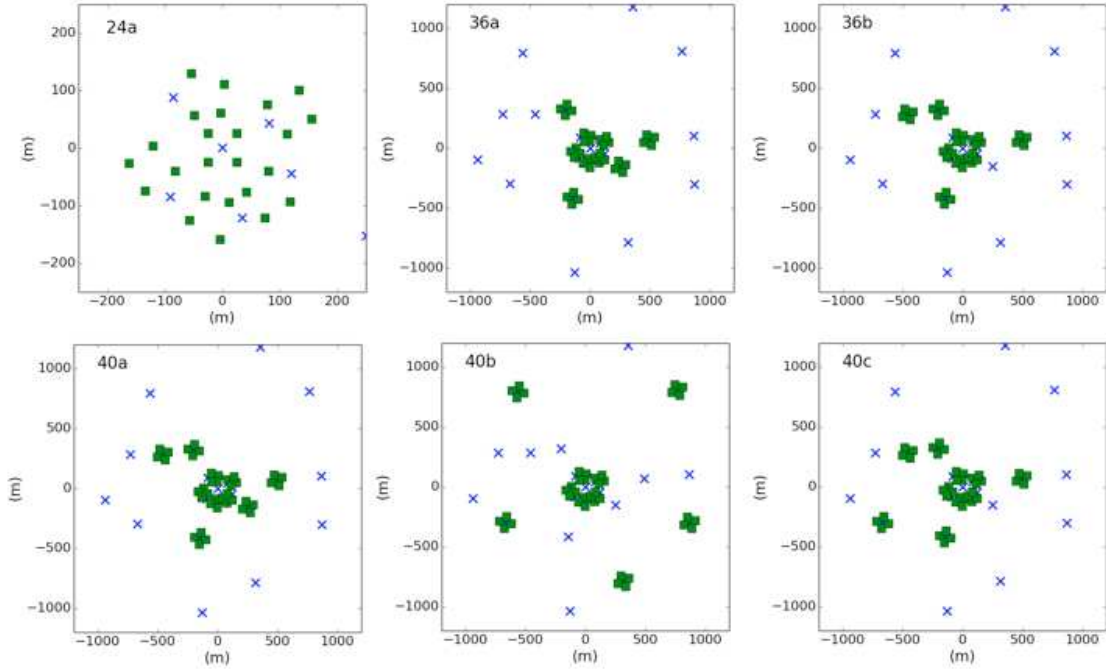


**Figure 4:** Arrangements of simulated LORA arrangements. Green squares represent scintillators, and blue crosses mark the center of LOFAR LBA stations. Notice the scale on arrangement 24a is different to show the infill of the current LORA arrangement.

For 19 energy bins between  $10^{15}$  eV and  $10^{19}$  eV, the probability of a minimum number of detectors having a signal is determined. This probability is multiplied by the cosmic ray flux in each energy bin. From this information, we study the trigger rate, triggered flux, and probability of triggering a minimum number of detectors. The aim is to increase the number of unbiased events above  $10^{16.5}$  eV, which are more likely to have a detectable radio signal, while maintaining the current event rate.

#### 4. Results

We first look at the expected trigger rate for each arrangement. The left panel of Figure 5 shows the trigger rate in Hz for a minimum number of detectors triggered. For example, the current trigger condition is 13 detectors with a signal, and the current trigger rate is  $\sim 0.8$  events/hour. LORA stations outside the superterp have 4 scintillators each, so when the trigger condition is 4 or fewer, the trigger rate for arrangements with more stations increases, while 24a remains similar to the current LORA rate. As the trigger condition increases, 24a has a high trigger rate than

the others, since one air shower that triggers at least 8 detectors will likely also include the infill. The conclusion is that the trigger rate for any LORA extension remains manageable, although the trigger condition may need to be increased.

Secondly, we look at the number of cosmic rays that will be detectable in different energy bins. The right panel of Figure 5 shows the triggered flux multiplied by energy for different arrangements. Since the flux depends on the trigger conditions, here we have used the condition that keeps the trigger rate at 1 event/hour. For condition 24a, 36a, and 40b it is 15 detectors. For 36b, and 40c this is 13 detectors, and for the current set up and 40a it is 12 detectors. Arrangement 24a collects a larger flux at low energies and offers no more improvements at high energies. Arrangement 40b, which is the option featuring the most widely spread out stations, performs similarly to LORA at low energies and then shows an improvement at the highest energies, where the particle footprint is large enough to encompass all the detectors. Arrangements 40c, 40a, 36a, and 36b show improvement in the whole range from  $10^{16}$  to  $10^{18}$  eV, with 40c performing the best.

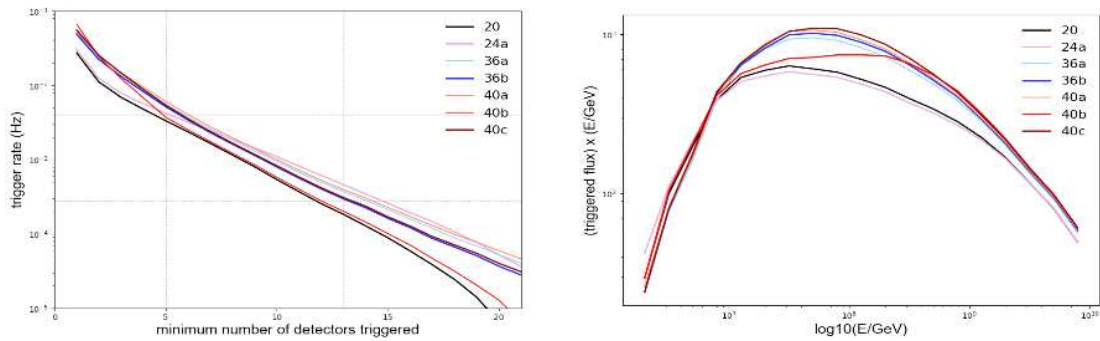


**Figure 5:** Left: Event rate for a minimum number of detectors required for a trigger. Right: CR flux multiplied by the probability of triggering. The trigger condition is chosen to keep the rate under 1 event per hour, and so different detector arrangements have different conditions.

Finally, we look at the probability of detection for different trigger conditions. For an area of 250 m around the center of the superterp, where 95% of event cores are currently located, the probability of detecting proton and iron showers between  $10^{16.4}$  and  $10^{16.6}$  eV is shown in Figure 6. This is the lowest energy band of interest, and higher energies will already have less intrinsic bias. Only arrangements 24a, 36b, and 40c are shown. At a trigger condition of 13 out of 20 detectors, an increase in probability of detection is already evident, particularly for zenith angles below  $30^\circ$ . Again, since not all cores are contained in the 250 m radius, it is necessary to determine bias on a case by case basis, however, increasing the probability of detection for both heavy and light primaries lessens the chance of a biased detection.

## 5. Science Outlook

Considering the cases of arrangements 24a, 36b, and 40c, we can determine the increase in events above  $10^{16.5}$  eV. Table 1 contains the percentage of simulated, triggered events above  $10^{16.5}$  eV based on the trigger condition that yields one event per hour, and the percent increase over the current LORA performance. The 24a detector arrangement performs worse than the cur-

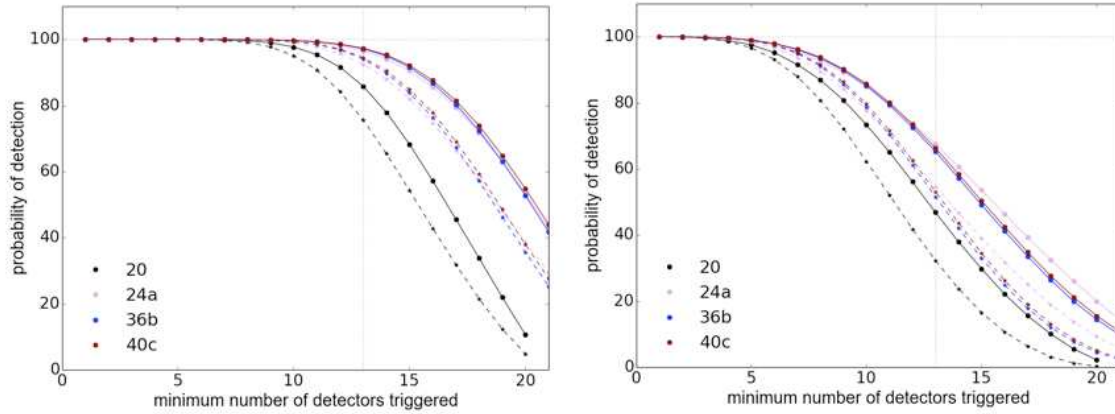


**Figure 6:** Probability of triggering a minimum number of detectors. Solid lines represent proton and dashed represent iron. Left: Zenith angles between  $0^\circ$  and  $30^\circ$ . Right: Zenith angles between  $30^\circ$  and  $45^\circ$ . The different colors represent different detector arrangements, all in the energy bin  $10^{16.4}$ - $10^{16.5}$ .

rent set up, as lower energy showers show a signal in more detectors. The 36b and 40c arrangements both have a significant increase in good events.

Det. Arr.	% good events	% increase
20	19.0	0
24a	17.3	-10
36b	26.7	40.5
40c	27.6	45.3

**Table 1:** Percentage of triggered events above  $10^{16.5}$  eV, and the percent increase over current performance.

In addition to the increase in good events, there is other scientific value in expanding LORA. Showers with cores outside the superterp will trigger LOFAR, which allows the dense antenna area in the superterp to sample the fringes of the radio footprint. Since the radio emission outside the Cherenkov cone is less compressed there, the radio pulses contain information about the early development of the shower. Additionally, more complicated trigger algorithms are possible. For example, requiring a specific subset of detectors to contain a signal, rather than a simple minimum number of detectors, allows for the possibility of triggering on specific shower geometries with desirable qualities for radio emission, such as larger zenith angles where the radio footprint is broader. In summery, the expansion of LORA increases the amount of data with a quality radio signal, and offers further possibilities of probing the radio footprint.

## 6. Acknowledgements

The LOFAR cosmic ray key science project acknowledges funding from an Advanced Grant of the European Research Council (FP/2007-2013) / ERC Grant Agreement n. 227610. The project has also received funding from the European Research Council (ERC) under the European Union’s Horizon 2020 research and innovation programme (grant agreement No 640130).

We furthermore acknowledge financial support from FOM, (FOM-project 12PR3041-3) and NWO (Top Grant 614-001-454, and Spinoza Prize SPI 78-409). AN is supported by the DFG (research fellowship NE 2031/1-1).

LOFAR, the Low Frequency Array designed and constructed by ASTRON, has facilities in several countries, that are owned by various parties (each with their own funding sources), and that are collectively operated by the International LOFAR Telescope foundation under a joint scientific policy.

## References

- [1] Tim Huege. Radio detection of cosmic ray air showers in the digital era. *Physics Reports*, 620:1–52, 2016.
- [2] S. Buitink et al. Method for high precision reconstruction of air shower  $X_{\max}$  using two-dimensional radio intensity profiles. *Phys. Rev. D*, 90(8), 2014.
- [3] P. Schellart et al. Detecting cosmic rays with the LOFAR radio telescope. *Astronomy and Astrophysics*, 560(A98), 2013.
- [4] M. P. van Haarlem et al. LOFAR: The LOW-Frequency ARray. *Astronomy and Astrophysics*, 556:56, 2013.
- [5] S. Thoudam et al. LORA: A scintillator array for LOFAR to measure extensive air showers. *Nucl.Instrum.Meth*, A767:339–346, 2014.
- [6] S. Thoudam et al. Measurement of the cosmic-ray energy spectrum above  $10^{16}$  eV with the LOFAR Radboud Air Shower Array. *Astroparticle Physics*, 73:34–43, 2016.
- [7] T. Antoni et al. (KASCADE Collaboration). The cosmic-ray experiment KASCADE. *Nuclear Instruments and Methods A*, 513:490, 2003.
- [8] A. Nelles et al. A parameterization for the radio emission of air showers as predicted by CoREAS simulations and applied to LOFAR measurements. *Astropart.Phys.*, 60:13–24, 2015.
- [9] D. Heck et al. CORSIKA: A Monte Carlo code to simulate extensive air showers. *Report FZKA*, 6019, 1998.
- [10] S. Ostapchenko. Monte Carlo treatment of hadronic interactions in enhanced Pomeron scheme: QGSJET-II model. *Phys. Rev. D*, 83(014018), 2011.
- [11] A. Ferrari et al. FLUKA: a multi-particle transport code. *CERN-2005-10*, INFN/TC\_05/11, 2005.
- [12] M. Koba et al. (Pierre Auger Collaboration). A thinning method using weight limitation for air-shower simulations. *Astropart.Phys.*, 15:259–273, 2001.
- [13] S. Agostinelli et al. GEANT4 –a simulation toolkit. *NIMPA*, 506(3):250–303, 2003.

# Overview and Status of the Lunar Detection of Cosmic Particles with LOFAR

---

**T. Winchen<sup>1\*</sup>, A. Bonardi<sup>2</sup>, S. Buitink<sup>1</sup>, A. Corstanje<sup>2</sup>, H. Falcke<sup>2,3,4</sup>, B. M. Hare<sup>5</sup>, J. R. Hörandel<sup>2,3</sup>, P. Mitra<sup>1</sup>, K. Mulrey<sup>1</sup>, A. Nelles<sup>2,6</sup>, J. P. Rachen<sup>2</sup>, L. Rossetto<sup>2</sup>, P. Schellart<sup>2,7</sup>, O. Scholten<sup>5,8</sup>, S. ter Veen<sup>2,4</sup>, S. Thoudam<sup>2,9</sup>, T. N. G. Trinh<sup>5</sup>**

<sup>1</sup> *Astrophysical Institute, Vrije Universiteit Brussel, Pleinlaan 2, 1050 Brussels, Belgium,*

<sup>2</sup> *Department of Astrophysics/IMAPP, Radboud University, P.O. Box 9010, 6500 GL Nijmegen, The Netherlands,*

<sup>3</sup> *NIKHEF, Science Park Amsterdam, 1098 XG Amsterdam, The Netherlands,*

<sup>4</sup> *Netherlands Institute of Radio Astronomy (ASTRON), Postbus 2, 7990 AA Dwingeloo, The Netherlands,*

<sup>5</sup> *KVI-CART, University Groningen, P.O. Box 72, 9700 AB Groningen,*

<sup>6</sup> *Department of Physics and Astronomy, University of California Irvine, Irvine, CA 92697-4575, USA,*

<sup>7</sup> *Department of Astrophysical Sciences, Princeton University, Princeton, NJ 08544, USA,*

<sup>8</sup> *Interuniversity Institute for High-Energy, Vrije Universiteit Brussel, Pleinlaan 2, 1050 Brussels, Belgium,*

<sup>9</sup> *Department of Physics and Electrical Engineering, Linnéuniversitetet, 35195 Växjö, Sweden*  
*E-mail: [tobias.winchen@rwth-aachen.de](mailto:tobias.winchen@rwth-aachen.de)*

When a cosmic particle hits matter it produces radio emission via the Askaryan effect. This allows to use Earth's moon as detector for cosmic particles by searching for these ns-pulses with radio telescopes. This technique potentially increases the available collective area by several orders of magnitude compared to current experiments. The LOw Frequency ARray (LOFAR) is the largest radio telescope operating in the optimum frequency regime for corresponding searches. In this contribution, we report on the design and status of the implementation of the lunar detection mode at LOFAR.

*35th International Cosmic Ray Conference — ICRC2017  
10–20 July, 2017  
Bexco, Busan, Korea*

---

\*Speaker.

## 1. Introduction

The low intensity of the cosmic-ray flux at the highest energies (UHECR) is one of the major challenges in answering the long standing open questions about their origin, acceleration, and composition (e.g. [1]). The same challenge arises in testing specific theories on super heavy dark matter [2, 3] and grand-unification [4] that predict an even lower flux of neutrinos with energies beyond the Zetta-eV scale. Even the largest currently operating cosmic-ray experiments [5, 6] detect only dozens of the highest energy particles per year, but cover already areas on the scale of small nations. It is thus doubtful, that experiments with an increase of more than an order of magnitude in sensitive volume can be realized on Earth.

Searching beyond Earth's atmosphere, a possible detector volume may be provided by Earth's moon, as particle interactions in the lunar rock emit a radio signal emitted by the Askaryan effect [7]. These radio signals can be recorded by an antenna array on the Moon's surface, or possibly cheaper with by radio-observatories on Earth [8]. Previous searches with Earth-bound radio telescopes have established only upper limits on the ZeV-scale neutrino flux, and have not been sensitive enough to constrain underlying production models or to observe UHECR [9–13].

An important limiting factor for these experiments is the frequency range of the used telescopes. While at GHz frequencies the expected pulse amplitude reaches a maximum, the pulse cannot escape the moon on most of its surface. The high frequencies are strongly beamed in direction of the Cherenkov angle, while the lower frequencies are emitted in a broader cone. As the critical angle of total internal reflection is identical to the Cherenkov angle, only radiation which strikes the surface at an acute angle with respect to the surface normal is emitted by the Moon. The lower frequencies can thus reach Earth at a wider range of impact angles of the primary particle than the higher frequencies. Also, as the lunar rock is more transparent to lower frequencies, the diminished signal amplitude is greatly outweighed by the increase in effective detector volume. Together, this results in an improved sensitivity of searches with telescopes operating at lower frequencies compared to searches that used higher frequencies. The optimal frequency range for lunar observations thus includes frequencies just above approximately 100 MHz [14].

## 2. The LOW Frequency ARray

The currently largest telescope covering the optimal frequency range for lunar detection of cosmic particles is the LOW Frequency ARray (LOFAR) [15]. As the first fully digital radio telescope, LOFAR contains no moveable dishes, but consists of fixed antenna arrays whose signals are directed into beams by digital processing.

The antennas arrays are grouped into multiple stations distributed throughout the Netherlands and with additional stations in France, Germany, Poland, the United Kingdom, and Sweden. Twenty-four of the stations are located in a dense core with an diameter of approximately 2 km in the Netherlands. The additional stations are distributed with increasing distances to this core yielding a maximum baseline of 1292 km. However, for lunar particle detection only the core stations can be used, as the data has to be processed in realtime and only the core stations are connected sufficiently fast.

Each core station is equipped with fields of 96 low-band antennas (LBAs) with a frequency range from 10-90 MHz and fields of 192 high-band antennas (HBAs) with a frequency range from 110-240 MHz. The signal received by the antennas is sampled in intervals of 5 ns and copied to a ring buffer of 5 s length at antenna level before being processed further. The signals of the individual omni-directional antennas are then filtered into sub-bands by a polyphase filter (PPF) and combined into a single beam of approximately  $5^\circ$  width at 120 MHz per station pointing towards a user-defined direction in the sky. A selection of sub-bands is then transmitted to a computing cluster for further processing as e.g. combining the station beams into smaller ‘tied-array’ beams and integrating the signal over longer time spans. Each station thus assumes the role of a single dish in a classical radio telescope.

### 3. Lunar Detection of Cosmic Particles with LOFAR

The lunar detection of cosmic particles with LOFAR faces several technical challenges. To maximize the effective area the signals of multiple stations have to be combined. As this reduces the size of the individual beams, multiple beams are required to cover the entire Moon. As each station, respectively beam, produces data with a rate of more than  $6.4 \text{ Gbit s}^{-1}$ , analysis of the data in real-time is required as only selective storage of the data is possible. Signals originating from the moon are dispersed in the Earth’s atmosphere. Triggering on the amplitude of a pulse thus requires correction for the dispersion. The pulse from a particle interaction is of only ns duration. By the PPF the time-resolution of the signal is reduced from 5 ns to only about  $5 \mu\text{s}$  in the individual sub-bands. Therefore, the inversion of the PPF is required for the lunar detection of particles. However, the inversion is not a loss-less procedure. We therefore use the recovered ns resolution signal only to trigger the read-out of the Transient-Buffer-Boards containing the original ADC traces. The offline analysis will thus not be limited by the accuracy of the PPF inversion which may produce artefacts, but all realtime-processing, i.e. beamforming, PPF inversion, ionospheric de-dispersion, and triggering has to be done within 5 s.

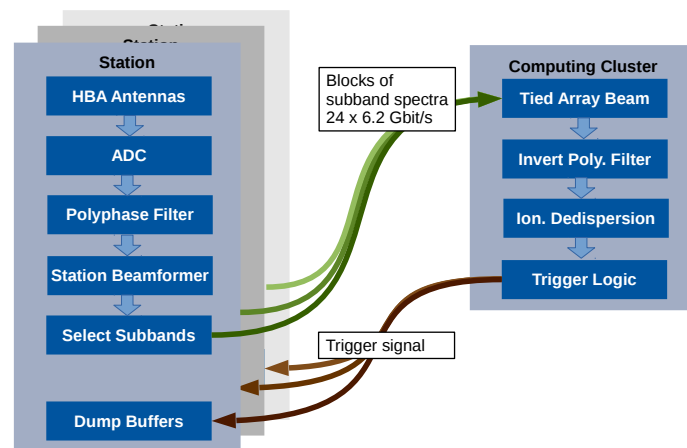


**Figure 1:** Overview of the online data analysis processing steps for the detection of ns-pulses with LOFAR [16].



The resulting sequence of the data processing steps necessary for the lunar detection of cosmic particles with LOFAR is sketched in figure 1. After transfer to the computing cluster, the station beams, each covering the full moon, will first be combined into multiple smaller beams, each focussed on a small fraction of the moon. The signal in ns resolution within each beam will then be recovered by inversion of the PPF, before the signal will be de-dispersed and eventually a trigger will be sent.

Prototypes for all necessary processing steps before the trigger have been developed. For the trigger we for now assume only a simple threshold excess. The real-time signal processing will require several thousand GFLOPs<sup>-1</sup> of computing power per beam. Here, inversion of the PPF is the most costly operation [17]. This required processing power is not available on the regular LOFAR processing machines, but the adjacent DRAGNET CPU/GPU cluster [18] designed for pulsar searches. However, the network connection limits the amount of data that can be processed in realtime on DRAGNET. Therefore a subset of 5–7 stations has to be selected for online analysis.

#### 4. Station Selection and Beam Properties

The choice of LOFAR stations defines the properties of the individual beams and herby the quality of the received signal. For lunar detection of cosmic particles, the following beam properties are desirable. As we can process 48 beams at maximum with the available computing power, the beam-size has to be symmetrical and of approx.  $0.5^\circ$  size to be able to cover the full moon.

As only 5 out of 48 substations can be used, 1712304 possible combinations exists which are too many to study individually in detail. However, based on the station position and orientation several combinations can be excluded without detailed simulation.

For LOFAR, the beam-size at wavelength  $\lambda$  can be estimated to

$$\Theta_{\text{FWHM}} = .8 \frac{\lambda}{L} \quad (4.1)$$

based on the maximum baseline between the stations  $L$  [15]. We consequently do not consider combinations with a maximum baseline below 1000 m and above 2000 m.

To achieve symmetry, the selected stations have to be arranged in a circular pattern as otherwise the beam-shape is also elongated. To quantify this behavior, we use the length of the resultant  $R = \frac{1}{N} \|\sum_i \vec{v}_i\|$  from the ensemble of station positions relative to the geometrical center of the subset of stations (cf. e.g. [19]).

In addition, the included baselines and station orientations should be uniformly distributed to minimize sidelobes. We again use the length of the resultant calculated from the station orientations to quantify the distribution of orientations. To quantify the uniformness of the distribution of baselines we use the standard Kolmogorov distance.

Using these variables as preselector, we calculated the beams of few selected combinations to find a suitable combination of stations. Figure 2 (a) shows the beam of a combination of stations that is acceptable in the maximum beam-size and has an above average uniformity of distribution of baselines, but has a directed distribution of beam-lines. Consequently the gain patterns are also directed, and several sidelobes are visible. The example beam shown in figure 2 (b) has good values also for the directions of the stations and beam-lines, resulting in asymmetric beam with few sidelobes. The corresponding stations are marked in the map of HBA stations shown in figure 3.

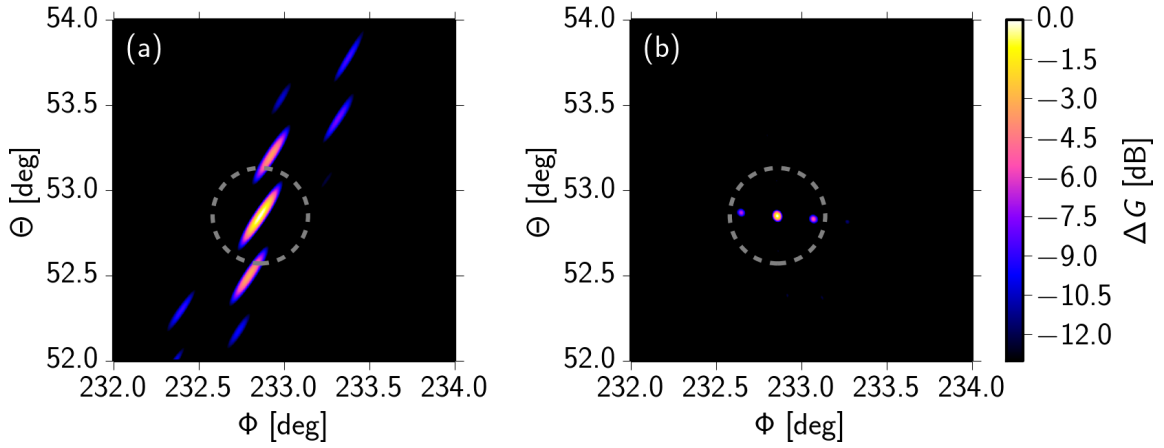


**Figure 2:** Example beams from different combinations of stations as indicated in figure 3. The dashed line marks the size of Earth's moon.

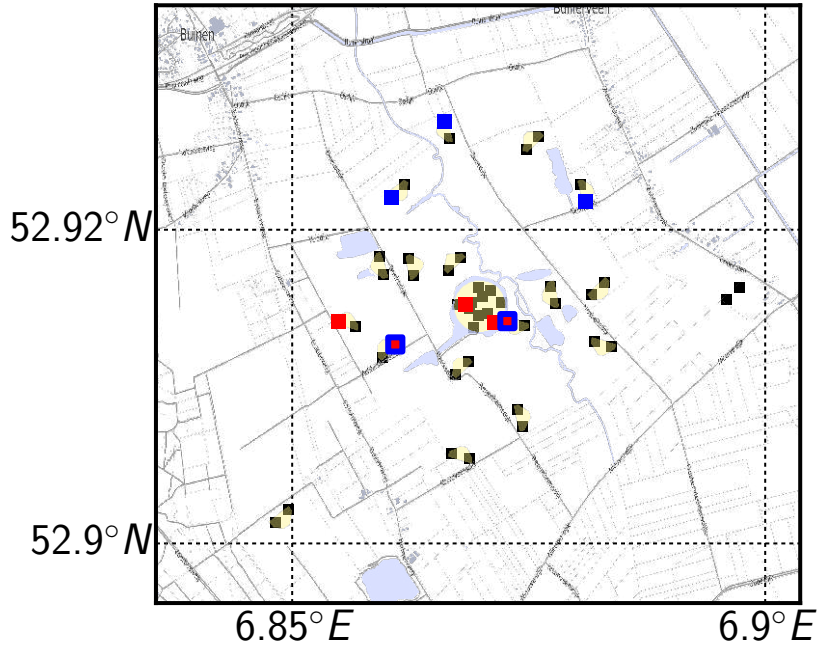


**Figure 3:** Map of the LOFAR core based on data by OpenStreetMap [20]. LOFAR HBA fields are marked with squares. Red markers correspond to station selection as in beam example fig. 2 (a), blue markers correspond to station selection as in beam example fig. 2 (b). Stations marked in black are not used in the examples.

The preselected combinations still have a large diversity in the properties of the beam and sidelobes. The final choice of stations will depend on the results of simulations of different trigger possibilities, with the achievable sensitivity as the deciding metric.

## 5. Expected Sensitivity

Currently, the best estimate of the expected sensitivity to cosmic particles with lunar obser-

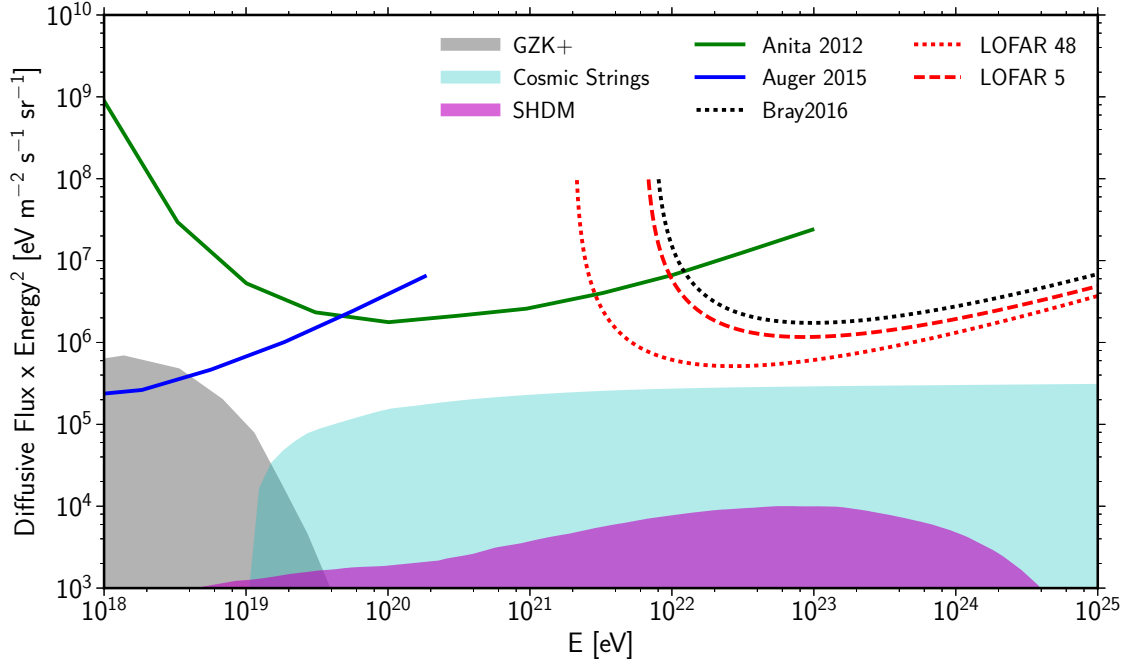


**Figure 4:** Existing limits (solid lines) on the flux of ultra high energetic neutrinos of previous observations [21, 22] and estimated limits for future observations (dashed and dotted lines). Model predictions for the flux of neutrinos from interaction of cosmic rays with background photons (GZK+) [23], cosmic strings [24], and super heavy dark matter (SHDM) [3] are marked as shaded areas.

variations is obtained following the procedure used in [25, 26]. Here, analytical approximations for multiple experiments are derived based on small angle approximations and constant transmission coefficients. While these approximations reproduce some features of early Monte Carlo simulations, the simplifications are valid only for large frequencies and may be in particular uncertain with the low observation frequencies used here. However, while the absolute scale of the sensitivity is uncertain, the approximation can be used to estimate the relevance of individual design choices.

In contrast to the revised calculation of the LOFAR sensitivity Bray 2016 [26], we here assume triggering on the coherently added polarizations and a trigger threshold  $n_\sigma = 6.4$  instead of  $n_\sigma = 12.4$  yielding a trigger rate of  $1 \text{ min}^{-1}$ . Furthermore, the previous estimate was based on a bandwidth of 48 MHz, while now 78.125 MHz can be used. The combined effect of these changes of parameters is shown assuming 5 and 48 substations in figure 4 for 200 h of observation. While the reduction of the total effective area to  $A_{\text{eff}} \approx 2150 \text{ m}$  for a moon elevation of  $56^\circ$  significantly reduces the expected sensitivity to using the full LOFAR array, the improved bandwidth and trigger assumptions still yield an improvement compared to the previous estimate.

## 6. Conclusion

Using the moon as detector that is read-out by Earth based radio telescopes still provides a chance to significantly increase the sensitive volume to detect high energetic cosmic particles.

However, conducting measurements with existing telescopes faces several technical challenges, as these instruments are not designed to operate on nano-second timescales. Nevertheless, observations with LOFAR, the currently most sensitive instrument, are currently in preparation. These observations can likely meet or exceed the previously estimated sensitivity.

## Acknowledgements

The LOFAR cosmic ray key science project acknowledges funding from an Advanced Grant of the European Research Council (FP/2007-2013) / ERC Grant Agreement n. 227610. The project has also received funding from the European Research Council (ERC) under the European Union's Horizon 2020 research and innovation programme (grant agreement No 640130). We furthermore acknowledge financial support from FOM, (FOM-project 12PR304) and NWO (VENI grant 639-041-130). LOFAR, the Low Frequency Array designed and constructed by ASTRON, has facilities in several countries, that are owned by various parties (each with their own funding sources), and that are collectively operated by the International LOFAR Telescope foundation under a joint scientific policy.

## References

- [1] K. Kotera and A. V. Olinto, *Annual Review of Astronomy and Astrophysics* **49**, 119–153 (2011), arXiv:1101.4256 [astro-ph.HE].
- [2] R. Aloisio, V. Berezhinsky, and M. Kachelriess, *Phys. Rev.* **D74**, 023516 (2006), arXiv:astro-ph/0604311 [astro-ph].
- [3] R. Aloisio, S. Matarrese, and A. V. Olinto, *JCAP* **1508**, 024 (2015), arXiv:1504.01319 [astro-ph.HE].
- [4] P. Bhattacharjee, [*AIP Conf. Proc.*433,168(1998)] (1997) 10.1063/1.56108, arXiv:astro-ph/9803029 [astro-ph].
- [5] A. Aab et al., *Nucl. Instrum. Meth.* **A798**, 172–213 (2015), arXiv:1502.01323 [astro-ph.IM].
- [6] H. Kawai et al., *Nuclear Physics B - Proceedings Supplements* **175**, Proceedings of the XIV International Symposium on Very High Energy Cosmic Ray Interactions, 221–226 (2008).
- [7] G. Askaryan, *Sovjet Physics J.E.T.P* **14**, 441 (1962).
- [8] R. D. Dagkesamanskij and I. M. Zheleznykh, *Soviet Journal of Experimental and Theoretical Physics Letters* **50**, 259–261 (1989).
- [9] S. Buitink et al., *Astron. Astrophys.* **521**, A47 (2010), arXiv:1004.0274 [astro-ph.HE].
- [10] T. H. Hankins, R. D. Ekers, and J. D. O'Sullivan, *Monthly Notices of the Royal Astronomical Society* **283**, 1027–1030 (1996).
- [11] C. W. James et al., *Mon. Not. Roy. Astron. Soc.* **410**, 885–889 (2011), arXiv:0906.3766 [astro-ph.HE].
- [12] C. W. James et al., *Mon. Not. Roy. Astron. Soc.* **379**, 1037–1041 (2007), arXiv:astro-ph/0702619 [astro-ph].

- [13] J. D. Bray et al., *Astropart. Phys.* **65**, 22–39 (2014), arXiv:1412.4418 [astro-ph.IM].
- [14] O. Scholten et al., *Astroparticle Physics* **26**, 219–229 (2006).
- [15] M. P. van Haarlem et al., *Astronomy and Astrophysics* **556**, A2 (2013), arXiv:1305.3550 [astro-ph.IM].
- [16] T. Winchen et al., *EPJ WoC* **135** (2017), arXiv:1609.06590.
- [17] T. Winchen et al., Accepted for publication in *JPCS* (2016), arXiv:1612.06592.
- [18] J. Hessels, *DRAGNET: a high-speed, wide-angle camera for catching extreme astrophysical events*, (Dec. 12, 2016) <http://www.astron.nl/dragnet>.
- [19] K. V. Mardia, *Statistics of directional data* (Academic Press, London, 1972).
- [20] OpenStreetMap contributors, *OSM Version 0.6*, (May 11, 2016) <https://www.openstreetmap.org>.
- [21] P. W. Gorham et al., *Phys. Rev. D* **85**, 049901 (2012).
- [22] A. Aab et al., *Phys. Rev.* **D91**, 092008 (2015), arXiv:1504.05397 [astro-ph.HE].
- [23] E. Roulet et al., *Journal of Cosmology and Astroparticle Physics* **1**, 028, 28 (2013), arXiv:1209.4033 [astro-ph.HE].
- [24] V. Berezhinsky, E. Sabancilar, and A. Vilenkin, *Phys. Rev.* **D84**, 085006 (2011), arXiv:1108.2509 [astro-ph.CO].
- [25] K. G. Gayley, R. L. Mutel, and T. R. Jaeger, *Astrophys. J.* **706**, 1556–1570 (2009), arXiv:0904.3389 [astro-ph.CO].
- [26] J. Bray, *Astroparticle Physics* **77**, 1–20 (2016), arXiv:1601.02980 [astro-ph.IM].